

Lunar seismology: An update on interior structure models

Raphael F. Garcia · Amir Khan · Mélanie
Drilleau · Ludovic Margerin · Taichi
Kawamura · Daoyuan Sun · Mark A.
Wieczorek · Attilio Rivoldini · Ceri
Nunn · Renee C. Weber · Angela G.
Marusiaak · Philippe Lognonné · Yosio
Nakamura · Peimin Zhu

Received: date / Accepted: date

R. F. Garcia (corresponding author)

Institut Supérieur de l'Aéronautique et de l'Espace (ISAE-SUPAERO), Université de Toulouse,
10 Ave E. Belin 31400 Toulouse, France

Tel.: +33-561338114

E-mail: raphael.garcia@isae.fr

Institut de Recherche en Astrophysique et Planétologie, C.N.R.S., Université de Toulouse, 14
Ave E. Belin, 31400 Toulouse, France

A. Khan

Institute of Geophysics, ETH Zürich, Switzerland.

M. Drilleau

Université de Paris, Institut de physique du globe de Paris, CNRS, F-75005 Paris, France

L. Margerin

Institut de Recherche en Astrophysique et Planétologie, C.N.R.S., Université de Toulouse, 14
Ave E. Belin, 31400 Toulouse, France

T. Kawamura

Institut de Physique du Globe de Paris, Paris, France

D. Sun

Laboratory of Seismology and Physics of Earths Interior, School of Earth and Space Sciences,
University of Science and Technology of China, Hefei, China
CAS Center for Excellence in Comparative Planetology, Hefei, China

M. A. Wieczorek

Université Côte d'Azur, Observatoire de la Côte d'Azur, CNRS, Laboratoire Lagrange, Nice,
France

A. Rivoldini

Observatoire Royal de Belgique, 3 Avenue Circulaire, 1050 Bruxelles, Belgique

C. Nunn

Jet Propulsion Laboratory - California Institute of Technology, Pasadena, U.S.A and Ludwig
Maximilian University, Munich, Germany

R. C. Weber

NASA Marshall Space Flight Center, Huntsville, AL, U.S.A.

A. G. Marusiaak

University of Maryland, College Park, MD, U.S.A.

1 **Abstract** An international team of researchers gathered, with the support of the
2 International Space Science Institute (ISSI), 1) to review seismological investiga-
3 tions of the lunar interior from the Apollo-era and up until the present and 2) to
4 re-assess our level of knowledge and uncertainty on the interior structure of the
5 Moon. A companion paper (Nunn et al., Submitted) reviews and discusses the
6 Apollo lunar seismic data with the aim of creating a new reference seismic data
7 set for future use by the community. In this study, we first review information
8 pertinent to the interior of the Moon that has become available since the Apollo
9 lunar landings, particularly in the past ten years, from orbiting spacecraft, con-
10 tinuing measurements, modeling studies, and laboratory experiments. Following
11 this, we discuss and compare a set of recent published models of the lunar inte-
12 rior, including a detailed review of attenuation and scattering properties of the
13 Moon. Common features and discrepancies between models and moonquake loca-
14 tions provide a first estimate of the error bars on the various seismic parameters.
15 Eventually, to assess the influence of model parameterisation and error propaga-
16 tion on inverted seismic velocity models, an inversion test is presented where three
17 different parameterisations are considered. For this purpose, we employ the travel
18 time data set gathered in our companion paper (Nunn et al., Submitted). The
19 error bars of the inverted seismic velocity models demonstrate that the Apollo lu-
20 nar seismic data mainly constrain the upper- and mid-mantle structure to a depth
21 of ~ 1200 km. While variable, there is some indication for an upper mantle low-
22 velocity zone (depth range 100–250 km), which is compatible with a temperature
23 gradient around $1.7^{\circ}\text{C}/\text{km}$. This upper mantle thermal gradient could be related
24 to the presence of the thermally anomalous region known as the Procellarum KREEP
25 Terrane, which contains a large amount of heat producing elements.

26 **1 Introduction**

27 Geophysical investigation of the Moon began with the manned Apollo lunar mis-
28 sions that deployed a host of instruments including seismometers, surface magne-
29 toimeters, heat-flow probes, retroreflectors, and a gravimeter on its surface. Much
30 of what we know today about the Moon comes from analysis of these data sets
31 that have and are continuously being complemented by new missions since the
32 Apollo era.

33 Of all of the geophysical methods, seismology provides the most detailed in-
34 formation because of its higher resolving power. Seismometers were deployed on
35 the lunar surface during each of the Apollo missions. Four of the seismic stations
36 (12, 14, 15, and 16), which were placed approximately in an equilateral triangle
37 (with corner distances of ~ 1100 km), operated simultaneously from December
38 1972 to September 1977. During this period, more than twelve thousand events

Y. Nakamura

Institute for Geophysics, John A. and Katherine G. Jackson School of Geosciences, University
of Texas at Austin, Austin, Texas, U.S.A.

P. Lognonné

Université de Paris, Institut de physique du globe de Paris, CNRS, F-75005 Paris, France

P. Zhu

China University of Geosciences, Wuhan, China

were recorded and catalogued with the long-period sensors including shallow and deep moonquakes and meteoroid and artificial impacts (e.g., Toksoz et al., 1974; Dainty et al., 1974; Lammlein, 1977; Nakamura, 1983). In addition, many more thermal quakes were also recorded with the short-period sensors (Duennebier and Sutton, 1974). That the Moon turned out to be so “active” came as somewhat of a surprise. A common notion prior to the lunar landings was partly reflected in Harold Urey’s belief that the Moon was a geologically dead body (Urey, 1952). At the time, only meteoroid impacts were expected to be recorded from which the internal structure of the Moon would be deduced. The existence of deep and shallow moonquakes was a serendipitous discovery – not accidental, but fortuitous and did much to improve models of lunar internal structure (see e.g., Nakamura, 2015, for a historical account).

The moonquakes are typically very small-magnitude events. The largest shallow moonquake has a body-wave magnitude of about 5, whereas the deep moonquakes have magnitudes less than 3 (Goins et al., 1981). That so many small-magnitude events could be observed at all is a combined result of the performance of the seismic sensors and the quiescence of the lunar environment, as neither an ocean nor an atmosphere is present to produce micro-seismic background noise.

The lunar seismic signals were found to be of long duration and high frequency content. These characteristics of lunar seismograms are related to intense scattering in a highly heterogeneous, dry, and porous lunar regolith and to low intrinsic attenuation of the lunar interior (this will be discussed in more detail in the following). This complexity, in combination with the scarcity of usable seismic events and small number of stations inevitably led to limitations on the information that could be obtained from the Apollo lunar seismic data (Toksoz et al., 1974; Goins, 1978; Nakamura, 1983; Khan and Mosegaard, 2002; Lognonné et al., 2003; Garcia et al., 2011). In spite of the “difficulties” that beset this data set, it nonetheless constitutes a unique resource from which several models of the lunar velocity structure have been and continue to be obtained. For this reason, it is considered important to gather the various processed data sets and published models and to synthesize our current knowledge of lunar internal structure in order to provide a broad access to this data set and models.

In addition to the seismic data, models of the lunar interior are also constrained by other geophysical data acquired during and after the Apollo missions – an endeavour that continues to this day either in-situ (through reflection of laser light on corner cube reflectors) or through orbiting satellite missions. These data, which are also considered in the following, include gravity and topography data, mass, moment of inertia, Love numbers (gravitational and shape response), electromagnetic sounding data and high pressure experiments that individually or in combination provide additional information on the deep lunar interior (Williams et al., 2001a; Zhong et al., 2012; Wieczorek et al., 2013; Shimizu et al., 2013; Williams et al., 2014; Besserer et al., 2014).

The authors of this paper are members of an international team that gathered in Bern and Beijing and were sponsored by the International Space Science Institute. The team convened for the purpose of gathering reference data sets and a set of reference lunar internal structural models of seismic wave speeds, density, attenuation and scattering properties. This work is summarized in two papers: this paper reviews and investigates lunar structural models based on geophysical data (seismic, geodetic, electromagnetic, dissipation-related) and the companion paper

(Nunn et al., Submitted) reviews the Apollo lunar seismic data. More specifically, in this study we compile and re-assess recent improvements in our knowledge of the lunar interior, including lunar geophysical data, models, and miscellaneous information that bears on this problem. All of these models embrace diverse parameterisations and data that are optimized for the purpose of addressing a specific issue. The question therefore arises as to the accuracy and consistency of the results if the different parameterisations are viewed from the point of view of a single unique data set. To address this issue, we re-investigate the problem of determining interior structure from the newly derived Apollo lunar seismic data described in our companion study (Nunn et al., Submitted) using a suite of different model parameterisations. For complimentary aspects of lunar geophysics, seismology, and interior structure, the reader is referred to reviews by Lognonné and Johnson (2007) and Khan et al. (2013).

2 Constraints on the lunar interior from geophysical observations, modeling studies, and laboratory measurements

2.1 Shape, Mass, Moment of inertia, and Love numbers

Radio tracking of lunar orbiting spacecraft, altimetry measurements from orbit, and analysis of Lunar Laser Ranging (LLR) data constrain a variety of global quantities that bear on the Moon's interior structure. These parameters include the average radius of the surface, the total mass, the moments of inertia of the solid portion of the Moon, and Love numbers that quantify tidal deformation.

The product of the lunar mass and gravitational constant GM is best determined by the Jet Propulsion Laboratory DE403 ephemeris (Williams et al., 2013) that is based on a combination of spacecraft and LLR data. This solution yields a value of the lunar mass of $M = (7.34630 \pm 0.00088) \times 10^{22}$ kg, where the uncertainty is dominated by the uncertainty in the gravitational constant (Williams et al., 2014). The shape of the Moon has been mapped by orbiting laser altimeters, of which the most successful was the instrument LOLA (Lunar Orbiter Laser Altimeter, Smith et al., 2010) that was flown on the Lunar Reconnaissance Orbiter (LRO) mission. The average radius R of the Moon from the LOLA data is 1737.151 km (Wieczorek, 2015), which is uncertain by less than 1 m. Combining these two quantities provides the average density of the Moon, which is $\bar{\rho} = 3345.56 \pm 0.40$ kg m^{-3} .

The response of the Moon to tides is quantified by Love numbers that depend upon the spherical harmonic degree and order of the tidal potential. The ratio of the induced potential to the tidal potential is given by the Love number k , whereas the ratio of the surface deformation to the tidal potential is proportional to the Love number h . For spherical harmonic degree 2, there are 5 independent Love numbers, and GRAIL analyses have solved for three of them: k_{20} , k_{21} and k_{22} (Konopliv et al., 2013; Lemoine et al., 2013) (the sine and cosine terms of the latter two were assumed to be equal). The three degree-2 Love numbers are approximately equal, and the uncertainty is reduced when solving only for a single value that is independent of angular order. Two independent analyses of the GRAIL data provide concordant values of $k_2 = 0.02405 \pm 0.00018$ (Konopliv et al., 2013) and $k_2 = 0.024116 \pm 0.000108$ (Lemoine et al., 2014). Following Williams

et al. (2014), we make use of an unweighted average of the two values and uncertainties, which yields $k_2 = 0.02408 \pm 0.00014$. Analyses of the GRAIL data also provide estimates of the degree-3 Love numbers, though with larger uncertainties: $k_3 = 0.0089 \pm 0.0021$ (Konopliv et al., 2013) and $k_3 = 0.00734 \pm 0.0015$ (Lemoine et al., 2013). It should be noted that the k_2 and k_3 Love numbers were calculated using a reference radius of $R_0 = 1738$ km. To obtain the corresponding values using the average radius of the Moon, it is necessary to multiply the k_2 values by $(R_0/R)^5$ and the k_3 values by $(R_0/R)^7$.

The moments of inertia of the Moon are uniquely determined by the large scale distribution of mass below the surface. Differences of the three principal moments are given by the degree-2 spherical harmonic coefficients of the gravitational potential. Ratios of the moments play an important role in quantifying time-variable physical libration signals that arise from tidal torques, and these can be determined from analyses of LLR data. The rotation of the Moon depends on the k_2 and h_2 Love numbers, the low degree spherical harmonic coefficients of the gravity field, and sources of energy dissipation. Two sources of energy dissipation have been found necessary to account for the LLR data: solid body dissipation as quantified by a frequency dependent quality factor Q , and viscous dissipation at the interface between a fluid core and solid mantle (see Williams et al., 2014; Williams and Boggs, 2015).

In the analyses of the LLR data, the absolute values of the moments of inertia of the fluid core are not well constrained. Nevertheless, differences between the core principal moments are detected, as is the viscous coupling constant. The moments of inertia of the solid portion of the Moon are tightly constrained, with an average value of $I_s/MR_0^2 = 0.392728 \pm 0.000012$ (Williams et al., 2014). Here, the average moment was normalized using a radius of $R_0 = 1738$ km, and to normalize the moments to the physical radius of the Moon, it is only necessary to multiply this value by $(R_0/R)^2$, which gives $I_s/MR^2 = 0.393112 \pm 0.000012$. Williams and Boggs (2015) constrain the quality factor to be $Q = 38 \pm 4$ at monthly periods and 41 ± 9 at yearly periods. The Q appears to increase for longer periods, but only lower bounds of 74 and 56 are obtained for periods of 3 and 6 years, respectively. Lastly, the LLR analyses constrain the monthly degree-2 Love number to be $h_2 = 0.0473 \pm 0.0061$. Independent analyses of orbital laser altimetry have been used to investigate the tidal response of the Moon. LOLA altimetric crossovers show a monthly signal that arises from tides, and this signal constrains the h_2 Love number to be 0.0371 ± 0.0033 (Mazarico et al., 2014), which is somewhat smaller than the value obtained from analyses of the LLR data.

The k_2 and h_2 Love numbers are in general frequency dependent. The orbital measurements are most sensitive to monthly periods and it has been recognized that there are non-negligible anelastic contributions to the Love numbers at these frequencies (e.g., Nimmo et al., 2012; Khan et al., 2014). When inverting for interior structure, it is convenient to estimate the purely elastic component in the infinite-frequency limit by removing the anelastic contribution. One technique that has been used to do so is to assume that the dissipation is both weak and frequency dependent with $Q \sim \omega^\alpha$, where ω is frequency and α is somewhere between 0.1 and 0.4 (e.g., Khan et al., 2014; Matsuyama et al., 2016).

Using the measured monthly values of k_2 and Q , the probability distribution of the predicted k_2 elastic Love number is plotted in Fig. 1 for four different values of α . The average value of the elastic k_2 is seen to increase from 0.206 to 0.232 as

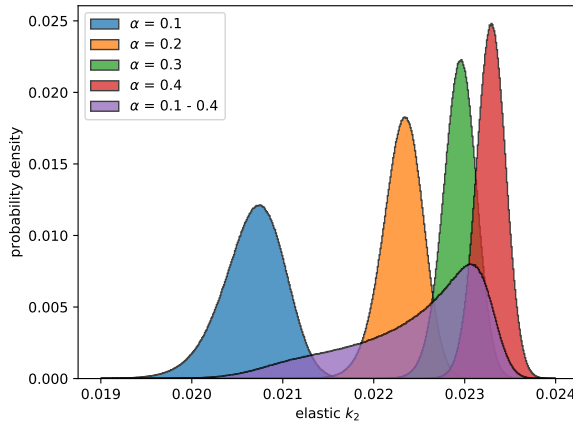


Fig. 1: Probability distributions of the elastic k_2 Love number for different values of α . Q is assumed to have a power law dependence on frequency with exponent α , and the distributions are plotted using constant values of 0.1, 0.2, 0.3, and 0.4. Also plotted is a case where all values of α from 0.1 to 0.4 are equally probable.

¹⁸² α increases from 0.1 to 0.4. Furthermore, the rate of change of the distributions
¹⁸³ decreases as α increases. If it is assumed that all values of α from 0.1 to 0.4
¹⁸⁴ are equally probable (as in Matsuyama et al., 2016), the distribution is found to
¹⁸⁵ be highly non-Gaussian, with a mode at 0.02307 and a 1σ confidence interval of
¹⁸⁶ [0.02169, 0.02316]. Using a value of $\alpha = 0.3$ (as in Khan et al., 2014), we find a
¹⁸⁷ value of 0.02294 ± 0.00018 . Anelastic corrections for the k_2 and h_2 Love number
¹⁸⁸ are presented in Table 5 using a value of $\alpha = 0.3$.

¹⁸⁹ 2.2 Crustal thickness, density, and porosity

¹⁹⁰ Analyses of high resolution gravity data from the GRAIL spacecraft have been able
¹⁹¹ to constrain the density and porosity of the lunar crust. The analysis procedure
¹⁹² makes use of the fact that short wavelength density variations in the crust generate
¹⁹³ gravity anomalies that rapidly attenuate with increasing depth below the surface,
¹⁹⁴ and that the gravitational signal of lithospheric flexure is unimportant for the
¹⁹⁵ shortest wavelengths. In the analysis of Wieczorek et al. (2013), it was assumed
¹⁹⁶ that the density of the crust was constant, and the bulk density was determined
¹⁹⁷ by the amplitude of the short wavelength gravity field. This approach provided an
¹⁹⁸ average bulk crustal density of 2550 kg m^{-3} , and when combined with estimates
¹⁹⁹ for the density of the minerals that compose the crust, this implies an average
²⁰⁰ porosity of about 12%.

²⁰¹ As a result of the assumptions employed in the above analysis, the bulk crustal
²⁰² density and porosity determinations should be considered to represent an average
²⁰³ over at least the upper few km of the crust. An alternative analysis that attempted
²⁰⁴ to constrain the depth dependence of density (Besserer et al., 2014) implies that
²⁰⁵ significant porosity exists several 10s of km beneath the surface. The closure of

pore space at depth was argued to occur primarily by viscous deformation (Wieczorek et al., 2013), which is a temperature dependent process. Using representative temperature gradients over the past 4 billion years, porosity is predicted to decrease rapidly over a narrow depth interval that lies somewhere between about 45 and 80 km depth. Thus, significant porosity could exist not only in the crust, but also in the uppermost mantle.

Lastly, we note that it is possible to invert for both the average thickness of the crust and lateral variations in crustal thickness using gravity and topography data (e.g., Wieczorek, 2015). These models, however, require knowledge of not only the density of the crust and mantle, but also an independent constraint on the crustal thickness at one or more locations. In the GRAIL-derived crustal thickness model of Wieczorek et al. (2013), the crustal thickness was constrained to be either 30 or 38 km in the vicinity of the Apollo 12 and 14 landing sites based on the seismic determinations of Lognonné et al. (2003) and Khan and Mosegaard (2002), respectively. The density of the mantle of this model was varied in order to achieve a crustal thickness close to zero in the center of the Crisium and Moscovense impact basins, which are both thought to have excavated through the crust and into the mantle (see Miljković et al., 2015). In these models, the average crustal thickness was found to be either 34 or 43 km, based on the thin and thick seismic determinations, respectively. In addition, the density of the uppermost mantle was constrained to lie between 3150 and 3360 kg m^{-3} , allowing for the possibility of a maximum of 6% porosity in the uppermost mantle.

2.3 Mantle temperature and electrical conductivity structure

Electromagnetic sounding data have been inverted to constrain the conductivity profile of the lunar interior (Sonett, 1982; Dyal et al., 1976; Hood et al., 1982; Hobbs et al., 1983), and have also been used to put limits on the present-day lunar temperature profile (Duba et al., 1976; Huebner et al., 1979; Hood et al., 1982; Khan et al., 2006b; Karato, 2013). Electromagnetic sounding data in the form of lunar day-side transfer functions (Hobbs et al., 1983) measure the lunar inductive response to external magnetic fields that change in time during intervals when the Moon is in the solar wind or terrestrial magnetosheath (Sonett, 1982). The transfer function data (Table 6) depend on frequency such that long-period signals are sensitive to deeper structure, while shorter periods sense the shallow structure. Limits on the lunar geotherm can be derived from the inferred bounds on the lunar electrical conductivity profile based on the observation that laboratory mineral conductivity measurements depend inversely on temperature.

Fig. 2a compiles the electrical conductivity models of Khan et al. (2014), Hood et al. (1982) and Karato (2013). The former is obtained from inversion of the lunar induction data described above and global geodetic data (M , I/MR^2 , and k_2) in combination with phase equilibrium modeling (see section 6.1 for more details), while the model of Hood et al. (1982) derives inversion of induction data only, whereas Karato (2013) combines Apollo-era electrical conductivity models with constraints from tidal dissipation (Q). When combined with mantle mineral electrical conductivity measurements, the phase equilibrium models (including density, seismic wave speed, and temperature profiles) can be turned into laboratory-based electrical conductivity models that can be tested against the available data. In con-

trast, Karato (2013) considers the mean Apollo-era conductivity profile derived by Hood et al. (1982) (dashed line in Fig. 2a) and tidal dissipation (Q) to constrain water and temperature distribution in the lunar mantle. Models are constructed on the basis of laboratory data and supplemented with theoretical models of the effect of water on conductivity and dissipative (anelastic) properties of the mantle. The conductivity models of Karato (2013) are generally consistent with an anhydrous mantle, although small amounts of water cannot be ruled out.

Current constraints on lunar mantle temperatures are shown in Fig. 2b in the form of a suite of present-day lunar thermal profiles. These derive from the geophysical studies of Khan et al. (2014), Karato (2013), and Kuskov and Kro-
nrod (2009). The latter study combines the seismic model of Nakamura (1983)
with phase equilibrium computations to convert the former to temperature given
various lunar bulk compositions. These studies indicate that present-day man-
tle temperatures are well below the mantle solidii of Longhi (2006) (also shown
in Fig. 2b) for depths ≤ 1000 km with average mantle thermal gradients of 0.5–
0.6 °C/km, corresponding to temperatures in the range $\sim 1000\text{--}1500$ °C at 1000
km depth. Larger thermal gradients of about 1°C/km were obtained in the same
depth range by Gagnepain-Beyneix et al. (2006). For depths > 1100 km, the man-
tle geotherms of Khan et al. (2014) and Karato (2013) (anhydrous case) cross the
solidii indicating the postential onset of melting in the deep lunar mantle and a
possible explanation for the observed tidal dissipation within the deep lunar inter-
ior observed by LLR (Williams et al., 2001b, 2014) (but see also Karato (2013)
and Nimmo et al. (2012) for alternative views).

Principal differences between the various models relate to differences in 1)
electrical conductivity database, including anhydrous versus hydrous conditions,
and 2) conductivity structure. Differences in laboratory electrical conductivity
measurements are discussed elsewhere (Karato, 2011; Yoshino, 2010; Yoshino and
Katsura, 2012), but the conductivity measurements of Karato are in general more
conductive than those of Yoshino and Katsura (Khan and Shankland, 2012). Be-
cause of the trade-off between water content and temperature on conductivity, the
hydrous cases considered by Karato (2013) result in lower mantle temperatures.
However, whether the lunar mantle is really hydrous remains an open question
(Hauri et al., 2015). Lastly, Karato (2013) employs the Apollo-era conductivity
model of Hood et al. (1982), which, overall, is less conductive in the upper 800 km
of the lunar mantle than the model of Khan et al. (2014). There is also evidence
for a partially molten lower mantle from geodetic and electromagnetic sounding
data (Khan et al., 2014), and to some extent the Apollo seismic data (Nakamura
et al., 1973; Nakamura, 2005; Weber et al., 2011).

290 2.4 Core

291 A partial liquid state of the lunar core or lower mantle is required to explain
292 the lunar laser ranging (LLR) measurements of the Moon's pole of rotation (e.g.
293 Williams et al., 2001b). Analysis of the seismic data have hinted at the presence
294 of a solid inner core (Weber et al., 2011), which, based on thermal evolution
295 modeling, appears necessary to explain the occurrence of the early lunar dynamo
296 (e.g., Laneuville et al., 2014; Scheinberg et al., 2015; Laneuville et al., 2019).
297 The conditions for either a liquid core or a solid-inner liquid-outer core to exist,

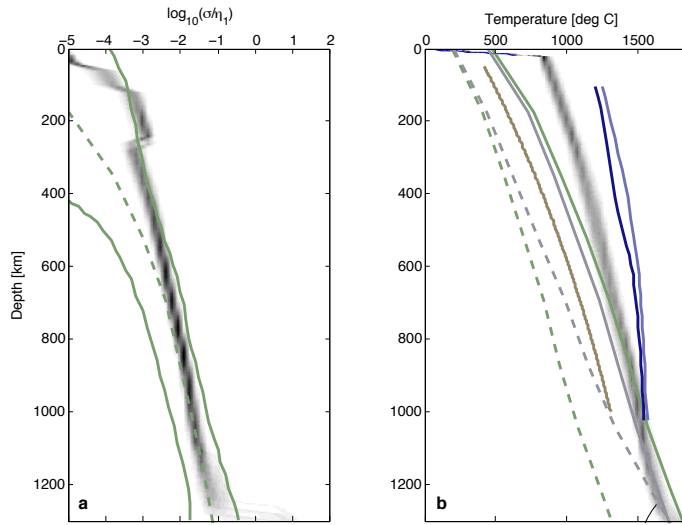


Fig. 2: Lunar mantle electrical conductivity (a) and thermal (b) profiles. In (a) green lines show the mean Apollo-era conductivity model and range of conductivities determined by Hood et al. (1982), whereas the contoured probability distributions are from Khan et al. (2014). In (b) the thermal profiles from Karato (2013) are based on dry olivine (solid gray line), dry orthopyroxene (solid green line), hydrous olivine (0.01 wt % H₂O, dashed gray line), and hydrous orthopyroxene (0.01 wt % H₂O, dashed green line). Contoured probability distributions are from Khan et al. (2014). Also included here is the lunar mantle geotherm of Kuskov and Kronrod (2009) and the solidi of Longhi (2006) for two lunar compositions: lunar primitive upper mantle (dark blue) and Taylor Whole Moon (light blue), respectively. $\eta_1=1$ S/m. Modified from Khan et al. (2014).

however, depend critically on the thermo-chemical conditions of the core. Table 1 compiles estimates of lunar core size and density that derive from geophysical data and modeling.

In order to allow for a present day liquid part in the core and to explain its average density (Table 1) light elements are required. The identity of those elements is still debated, but the most plausible candidates are carbon and sulfur. Evidence for sulfur or carbon is deduced from lunar surface samples, assumptions about the formation of the lunar core, and laboratory data about the partitioning of siderophile elements between silicate melts and liquid metal (e.g., Righter and Drake, 1996; Rai and van Westrenen, 2014; Chi et al., 2014; Steenstra et al., 2017; Righter et al., 2017). The presence of other light elements like silicon or oxygen in appreciable amounts is unlikely because of unfavorable redox conditions during core formation (e.g., Ricolleau et al., 2011). Both carbon and sulfur depress the melting temperature of iron significantly, allowing for a present-day liquid core (Fig. 3).

The density of liquid Fe-S and Fe-C as a function of light element concentration at lunar core pressures is shown in Fig. 3b. The density of liquid Fe-S has been calculated following Morard et al. (2018). For liquid Fe-C an ideal solution model

316 has been assumed with liquid Fe (Komabayashi, 2014) and liquid Fe3.5wt%C
 317 (Shimoyama et al., 2016) as end-members. Compared to Fe-S, the density of Fe-
 318 C decreases significantly slower with increasing light element concentration and
 319 the amount of C that can be dissolved in liquid Fe is below about 7 wt% at
 320 the pressure-temperature conditions of the lunar core, whereas sulfur saturation
 321 in Fe occurs at significantly larger concentrations. Consequently, if carbon were
 322 the major light element, then the average core density cannot be significantly
 323 lower than 7000 kg/m^3 . Moreover, a solid graphite layer could be present (Fei
 324 and Brosh, 2014) in the upper part of the core below the core-mantle-boundary,
 325 since temperature was higher when the core formed and therefore the C saturation
 326 concentration somewhat larger.

327 If instead the principal light element were sulfur, the average density of the
 328 core of the Moon (Table 1) implies that its concentration could be above 27 wt%.
 329 Such large amounts, however, appear to be at odds with lunar dynamo models
 330 that rely on the formation of an inner core that crystallises from the bottom-up
 331 to explain the timing of the past dynamo (e.g. Laneuville et al., 2014; Scheinberg
 332 et al., 2015). Depending on the precise amount of sulfur, different scenarios are
 333 possible for the core of the Moon. If, for example, the sulfur concentration is below
 334 the eutectic, i.e., <25 wt% (Fig. 3), then the core is likely be completely molten
 335 today, although a small inner core forming through precipitation of iron snow in
 336 the liquid part cannot be excluded. If, however, the S concentration is above the
 337 eutectic, then solid FeS will possibly crystallize and float to the top of the core.

338 Sulfur, however, appears to be disfavored by the most recent results based on
 339 thermo-chemical modeling (<0.5 wt%S) (Steenstra et al., 2017, 2018). Moreover,
 340 such sulfur-poor liquids, which correspond to densities around 7000 kg/m^3 , imply
 341 present-day core temperatures around 2000 K and, as a consequence, significantly
 342 higher and, very likely too high, temperatures earlier on (e.g., Laneuville et al.,
 343 2014; Scheinberg et al., 2015). Depending on the lower mantle solidus, the require-
 344 ment for either a molten or solid lower mantle, and the timing of the early lunar
 345 dynamo, the temperature at the core-mantle boundary has been estimated in the
 346 range $\sim 1500\text{--}1900 \text{ K}$. The lowest temperature in this range is below the Fe-C eu-
 347 tectic temperature at 5 GPa and would therefore imply a solid core if it were made
 348 of iron and carbon only. In comparison, present-day limits on the temperature of
 349 the deep lunar interior ($\sim 1100 \text{ km depth}$) suggest temperatures in excess of 1800 K
 350 (Fig. 2b).

351 **3 A short review of published seismic velocity and density models**

352 This section details some of the previously published models (those that are present
 353 in digital format). The specific data sets and prior information used to construct
 354 these models are summarized in Table 2. The amount of data used in the model
 355 inversions has noticeably increased with time. The tendency to include more global
 356 geophysical information (e.g., mass, moment of inertia, love numbers, electromag-
 357 netic sounding data) reflects the limitations inherent in the inversion of direct
 358 P- and S-wave arrival times in order to resolve lunar structure below $\sim 1200 \text{ km}$
 359 depth.

360 The seismic data collected during the 8 years that the lunar seismic stations
 361 were active have resulted in more than 12000 recorded events (Nunn et al., Sub-

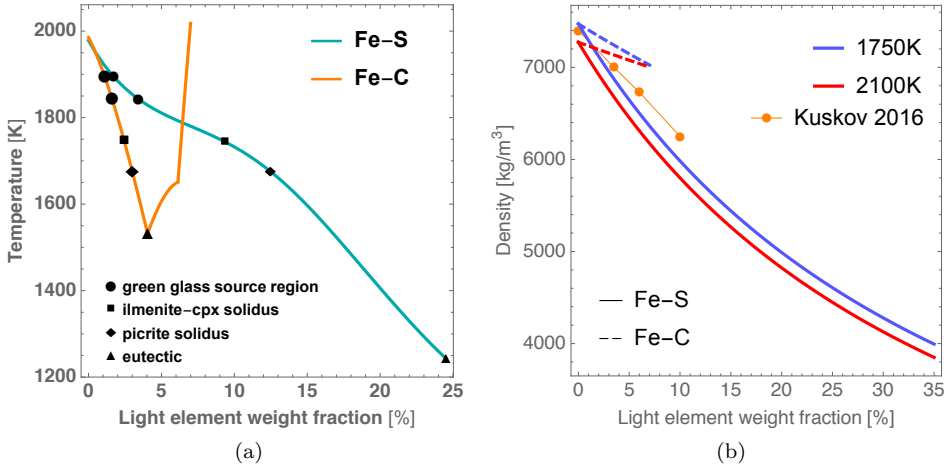


Fig. 3: Dependence of liquidus and density of Fe-S and Fe-C on light element content. (a) Iron-rich liquidus of Fe-S (Buono and Walker, 2011) and liquidus of Fe-C (Fei and Brosh, 2014) at 5 GPa. Symbols show candidate mantle solidi: green glass source (Longhi, 2006), ilmenite-cpx (Wyatt, 1977), picrite (Green et al., 1971), and the eutectic of Fe-S and Fe-C. (b) Density of liquid Fe-S and Fe-C at 5 GPa at two representative mantle temperatures (cf. Fig. 2b). The weight fraction of S is below the eutectic composition (~ 25 wt%) and that of C is below its saturation (~ 7 wt%). Orange circles are densities for Fe-S based on the molecular dynamics simulations of Kuskov and Belashchenko (2016) (at 5 GPa and 2000 K).

362 mitted) of which only a subset were used to infer the lunar velocity structure
 363 (summarized in Table 2). Based on the final Apollo-era analyses of the two event
 364 data sets then available (Goins et al., 1981; Nakamura, 1983), the major features
 365 of the lunar interior could be inferred to a depth of ~ 1100 km. More recent re-
 366 analysis of the Apollo lunar seismic data using modern analysis techniques (Khan
 367 and Mosegaard, 2002; Lognonné et al., 2003; Gagnepain-Beyneix et al., 2006) have
 368 largely confirmed earlier findings, but also added new insights (see below), while
 369 Nakamura (2005) expanded his original data set with an enlarged deep moonquake
 370 catalog.

371 In addition to the data obtained from the passive seismic experiment, active
 372 seismic experiments were also carried out during Apollo missions 14, 16, and 17
 373 with the purpose of imaging the crust beneath the various landing sites (Ko-
 374 vach and Watkins, 1973a,b; Cooper et al., 1974). The Apollo 17 mission carried a
 375 gravimeter that, because of instrumental difficulties, came to function as a short-
 376 period seismometer (Kawamura et al., 2015). Other seismological techniques to in-
 377 fer near-surface, crust, and deeper structure include analysis of receiver functions
 378 (Vinnik et al., 2001), noise cross-correlation (Larose et al., 2005; Sens-Schönfelder
 379 and Larose, 2008), seismic coda (Blanchette-Guertin et al., 2012; Gillet et al.,
 380 2017), array-based waveform stacking methods (Weber et al., 2011; Garcia et al.,

Table 1: Summary of lunar core size estimates, methods and data that have been used to constrain these. Abbreviations are as follows: $\rho_a(\omega)$ =frequency-dependent electromagnetic sounding data; M =mean mass; I/MR^2 =mean moment of inertia; k_2, h_2 =2nd degree Love numbers; Q =global tidal dissipation; T_P, T_S =lunar seismic travel times; LLR=lunar laser ranging. Note that although a number of studies are indicated as using the same data, there can nonetheless be modeling and processing differences between the various studies.

Core radius (km)	Core density (g/cm ³)	Data and/or Method	Source
170–360	–	Apollo T_P, T_S	Nakamura et al. (1974)
250–430	–	Lunar Prospector $\rho_a(\omega)$	Hood et al. (1999)
350–370	5.3–7	LLR data	Williams et al. (2001a)
350–400	6–7	$M, I/MR^2, k_2, Q$	Khan et al. (2004)
300–400	5–7	$M, I/MR^2, k_2, h_2, Q$	Khan and Mosegaard (2005)
340–350	5.7	$M, I/MR^2$, Apollo T_P, T_S	Khan et al. (2006a)
310–350	–	Apollo lunar seismograms	Weber et al. (2011)
340–420	4.2–6.2	Apollo T_P, T_S and seismograms, $M, I/MR^2, k_2$	Garcia et al. (2011)
310–370	5.7	Seismic model and $M, I/MR^2$	Kronrod and Kuskov (2011)
290–400	–	Kaguya and Lunar Prospector $\rho_a(\omega)$	Shimizu et al. (2013)
200–380	–	GRAIL gravity data and LLR	Williams et al. (2014)
330–380	4.5–5	Apollo $\rho_a(\omega), M, I/MR^2, k_2$	Khan et al. (2014)
330–400	3.9–5.5	$M, I/MR^2, k_2, Q$, Apollo T_P, T_S	Matsumoto et al. (2015)
<330	6–7.5	Molecular dynamics simulations of Fe-S (3–10 wt% S) alloys	Kuskov and Belashchenko (2016)
310–380	5.2–6.7	Elastic data of liquid Fe-S alloys (10–27wt% S)	Morard et al. (2018)

381 2011), and waveform analysis techniques based on spatial seismic wavefield gradients (Sollberger et al., 2016).

382 The one-dimensional seismic velocity and density models are compared in Fig.
383 4 and are provided as supplementary information in "named discontinuities" (nd)
384 format. The recent velocity models of Khan and Mosegaard (2002); Lognonné
385 et al. (2003); Gagnepain-Beyneix et al. (2006) are based on modern-day inversion
386 (Monte Carlo and random search) and analysis techniques. The models of Khan
387 and Mosegaard (2002), while relying on a Monte Carlo-based sampling algorithm
388 (Markov chain Monte Carlo method) to invert the same data set considered by
389 Nakamura (1983), provided more accurate error and resolution analysis than pos-
390 sible with the linearized methods available during the Apollo era. Lognonné et al.
391 (2003) and Gagnepain-Beyneix et al. (2006) first performed a complete reanalysis
392 of the entire data set to obtain independently-read arrival times and subsequently
393 inverted these using random search of the model space. In all of the above studies
394 both source location and internal structure were inverted for simultaneously.

395 Interpretation of Apollo-era seismic velocity models resulted in crustal thick-
396 nesses of 60 ± 5 km (Toksoz et al., 1974), but have decreased to 45 ± 5 km (Khan
397 et al., 2000), 38 ± 3 km (Khan and Mosegaard, 2002), and 30 ± 2.5 km (Lognonné
398 et al., 2003).

399 Differences in crustal thickness estimates between Apollo-era and recent models
400 are discussed in detail in Khan et al. (2013). They relate to the use of additional,
401 but highly uncertain, body wave data (amplitudes, secondary arrivals, synthetic
402 seismograms) in the seventies. Differences in crustal thickness between the recent
403 models of (Khan et al., 2000), (Khan and Mosegaard, 2002), and (Lognonné et al.,

405 2003) result from a combination of differences in travel time readings (data), inversion
406 technique (methodology), and model parameterisation. Vinnik et al. (2001)
407 also presented evidence for a shallower lunar crust-mantle boundary (28 km)
408 through detection of converted phases below Apollo station 12.

409 Moving below the crust, mantle seismic velocity models are generally consistent
410 to a depth of \sim 1200 km, which defines the bottoming depths of the direct
411 P- and S-wave arrivals emanating from the furthest events that include a far-side
412 meteoroid impact and a deep moonquake nest (A33). In an attempt to obtain
413 more information on density and the deeper interior (e.g., core size and density),
414 more elaborate approaches to inverting the arrival time data set have been con-
415 sidered. These include adding geodetic and electromagnetic sounding data, use of
416 equation-of-state models, and petrological information (Khan et al., 2007; Khan
417 et al., 2014; Garcia et al., 2011; Matsumoto et al., 2015). While these studies have
418 provided insights on the deep lunar interior, particularly mantle density structure,
419 it has proved difficult to tightly constrain core size and density on account of the
420 smallness of the core.

421 Khan et al. (2006a) computed petrological phase equilibria using Gibbs free en-
422 ergy minimization techniques (Connolly, 2009), which were combined with stochas-
423 tic inversion. Briefly, stable mineral phases, their modes and physical proper-
424 ties (P-, S-wave velocity and density) were computed as a function of temper-
425 ature and pressure within the CFMAS system (comprising oxides of the ele-
426 ments CaO,FeO,MgO,Al₂O₃,SiO₂). By inverting the seismic travel time data set
427 of Lognonné et al. (2003) jointly with lunar mass and moment of inertia, while
428 assuming crust and mantle to be compositionally uniform, they determined the
429 compositional range of the oxide elements, thermal state, Mg#, mineralogy, phys-
430 ical structure of the lunar interior, and core size and density.

431 Garcia et al. (2011) inverted the travel time data of Lognonné et al. (2003)
432 and mass and moment of inertia using the simplified Adams-Williamson equation
433 of state. The latter assumes adiabatic compression of an isochemical material
434 devoid of any mineral phase changes, coupled with a Birch-type linear relationship
435 between seismic velocity and density. Garcia et al. (2011) also considered core
436 reflected phases in an attempt to determine core size. While core reflections were
437 allegedly observed by Garcia et al. (2011) and Weber et al. (2011), it has to be
438 noted that the resultant core size estimates differ largely because of differences
439 in mantle seismic velocities. Garcia et al. (2011) favor a core with a radius of
440 380 ± 40 km with an outer liquid part, while Weber et al. (2011) find a 150 km
441 thick partially molten mantle layer overlying a 330 km radius core, whose outer
442 90 km is liquid.

443 Matsumoto et al. (2015) jointly inverted the travel time data of Lognonné et al.
444 (2003) (event parameters were fixed), mean mass and moment of inertia, and tidal
445 response (k_2 and Q) for models of elastic parameters (shear and bulk modulus),
446 density, and viscosity within a number of layers. Viscosity was included as param-
447 eter in connection with a Maxwell viscoelastic model following the approach of
448 Harada et al. (2014). Evidence for a lower mantle low-velocity layer (depth range
449 1200–1400 km) and a potentially molten or fully liquid core (330 km in radius)
450 was found.

451 Finally, all available geophysical data and model interpretations are consistent
452 with a Moon that has differentiated into a silicate crust and mantle and an Fe-rich
453 core (e.g., Hood, 1986; Hood and Zuber, 2000; Wieczorek et al., 2006; Khan et al.,

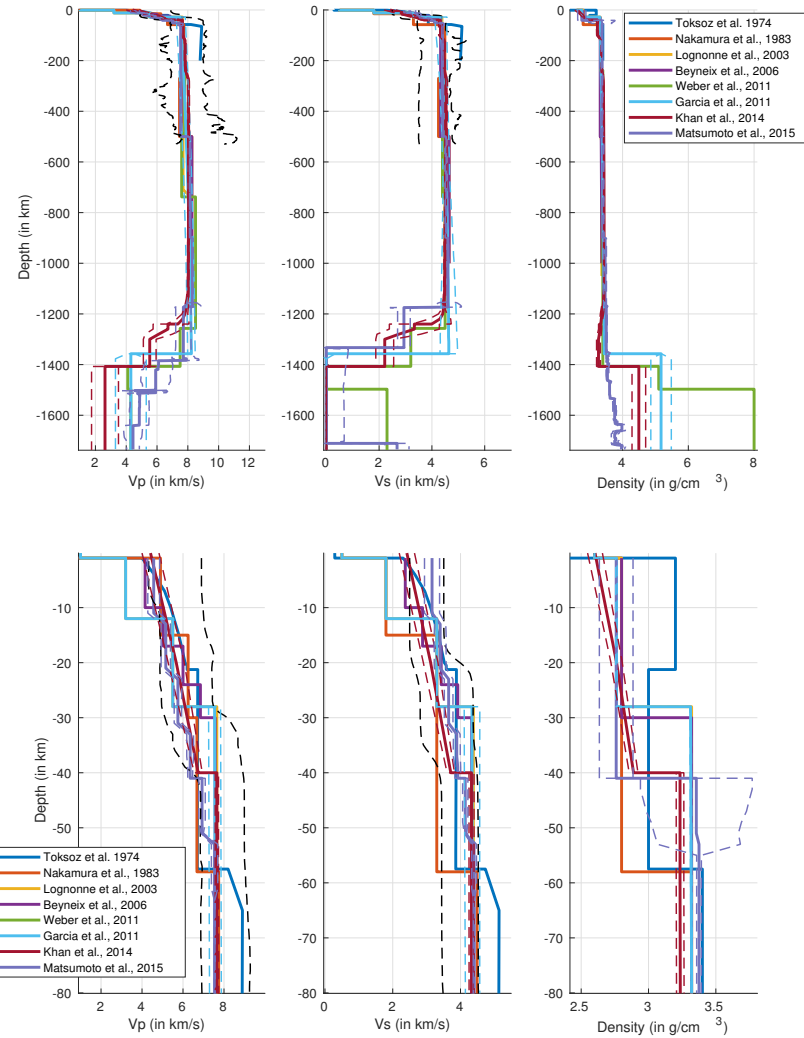


Fig. 4: Comparison of previously published lunar seismic velocity models. Radial profiles of P-wave velocity on the left, S-wave velocity in the center, and density on the right are presented from the surface to center of the Moon (top) and a zoom on crust and uppermost mantle (bottom). Solid lines indicate either mean or most likely model for each study, dashed lines indicate one standard deviation error bar where available. Black dashed lines indicate the contour lines including half of the model distribution with highest probability density in Khan and Mosegaard (2002), limited to the first 500 km of the Moon.

2013). Our current view of the lunar interior is summarised in Fig. 5. Evidence for a mid-mantle discontinuity separating the mantle into upper and lower parts is uncertain (Nakamura, 1983; Khan and Mosegaard, 2002), but there is evidence for the presence of partial melt at depth based on analysis of characteristics of farside seismic signals (absence of detectable S-waves) (Nakamura et al., 1973; Sellers, 1992; Nakamura, 2005) and the long-period tidal response of the Moon (e.g., Williams et al., 2001a; Khan et al., 2004; Efroimsky, 2012b,a; van Kan Parker et al., 2012; Khan et al., 2014; Harada et al., 2014). This presence of melt is still debated within the authors of this paper because the above two evidences can also be reproduced by a low viscosity layer not requiring melt (Nimmo et al., 2012). Owing to the distribution of the seismic sources observed on the Moon, the deep interior has been more difficult to image, but the overall evidence suggests that the Moon has a small core with a radius in the range 300–350 km that is most probably either partially or entirely molten (Weber et al., 2011; Garcia et al., 2011). Absence of clear detection of farside deep moonquakes (if located in the deep moonquake shadow zone) seems to support this further (Nakamura, 2005). While direct evidence for a solid inner core is highly uncertain, it could be present if a portion of the liquid core has crystallised but will depend crucially on its composition as discussed earlier (section 2.4). Current geophysical constraints on core density estimates do not uniquely constrain composition, but are in favor of a core composed mainly of iron with some additional light elements (e.g., Fei and Brosh, 2014; Antonangeli et al., 2015; Shimoyama et al., 2016; Kuskov and Belashchenko, 2016; Morard et al., 2018) (see section 2.4). Support for an iron-rich core is also provided by recent measurements of sound velocities of iron alloys at lunar core conditions (e.g., Jing et al., 2014; Nishida et al., 2016; Shimoyama et al., 2016), although the density of these alloys is much higher than those deduced for the core from geophysical data.

4 Seismic scattering and attenuation models

This section summarizes the main findings on the scattering and absorption properties of the Moon. Lunar Q estimates are summarized in Table 3.

4.1 Basic definitions and observations

In seismology, attenuation refers to the (exponential) decay of the amplitude of ballistic waves with distance from the source after correction for geometrical spreading and site effects. The two basic mechanisms at the origin of seismic attenuation are energy dissipation caused by anelastic processes and scattering by small-scale heterogeneities of the medium. Each of these mechanisms may be quantified with the aid of a quality factor Q equal to the relative loss of energy of the propagating wave per cycle. In comparison with their terrestrial counterparts, a striking feature of lunar seismograms is the long ringing coda that can last for more than an hour. This is understood as the result of intense scattering in the mega-regolith layer and the extremely low dissipation on the Moon compared to the Earth. Scattering removes energy from the coherent ballistic waves and redistributes it in the form of diffuse waves that compose the seismic signal known as coda. In the case of the

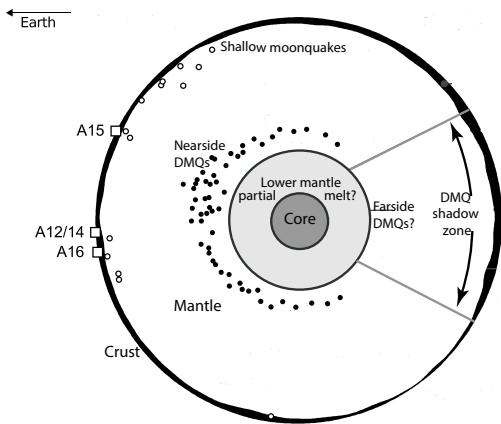


Fig. 5: Schematic diagram of lunar internal structure as seen by a host of geo-physical data and models. The Moon has differentiated into crust, mantle, and core with no clear indication for a mid-mantle division, but considerable evidence for a partially molten lower mantle. The core is most likely liquid and made of Fe with a light element (e.g., S or C) with a radius ≤ 350 km. Presence of a solid inner core is highly uncertain and therefore not indicated. Apollo stations are indicated by A12–A16 and are all located on the nearside of the Moon. Shallow and deep (DMQ) moonquakes occur in the depth ranges 50–200 km and 800–1100 km, respectively. See main text for more details. Modified from Khan et al. (2014).

497 Moon, scattering is so strong as to cause a delay of the order of several hundreds
 498 of seconds between the onset of the signal and the arrival time of the maximum
 499 of the energy. This delay time t_d is a useful characteristics of lunar seismograms
 500 and measurements have been reported in several studies (see e.g. Dainty et al.,
 501 1974; Gillet et al., 2017). The extreme broadening of lunar seismograms was in-
 502 terpreted by Latham et al. (1970a) as a marker of the diffusion of seismic energy
 503 in the lunar interior, a physical model which still prevails today. For this reason,
 504 the strength of scattering in the Moon is most often quantified by a diffusion con-
 505 stant D (expressed in km^2/s) and we shall adhere to this convention (low/high
 506 diffusivity corresponding to strong/weak scattering). The notation Q will be em-
 507 ployed to denote attenuation due to dissipation processes. The rate of decay of
 508 seismograms in the time domain is yet another useful characteristic which may be
 509 quantified with the aid of a quality factor, which we shall label Q_c . In the diffusion
 510 (multiple scattering) regime, Q_c may be used as proxy for Q in the case of strong
 511 stratification of heterogeneity (Aki and Chouet, 1975). First attempts to estimate
 512 Q from the coda decay were carried out shortly after the deployment of Apollo
 513 seismometers. Using data from the artificial impacts, Latham et al. (1970a) and
 514 Latham et al. (1970b) found the Q of the upper crust to be in the range 3000–3600.
 515 Before discussing these measurements in more detail we briefly review dissipation
 516 estimates from lunar rock samples using acoustic sounding.

517 4.2 Q measurements of lunar samples in the laboratory

518 Early experimental measurements of dissipation in lunar rock samples by Kanamori
519 et al. (1970) and Wang et al. (1971) were in sharp contradiction with the first in-
520 situ seismic observations of Latham et al. (1970a,b). Kanamori et al. (1970) and
521 Wang et al. (1971) reported extremely low $Q \approx 10$ at 1MHz – more than 2 orders
522 of magnitude less than the seismically determined Q – using basic pulse trans-
523 mission experiments. Besides the low accuracy of these measurements, the very
524 high-frequency at which they were performed questioned the validity of their inter-
525 pretation in terms of dissipation, since scattering might be efficient around 1MHz.
526 More accurate estimates by Warren et al. (1971) based on the resonance mode
527 of a vibrating bar around 70kHz reduced the discrepancy by roughly one order
528 of magnitude, but still left a gap with regard to the seismic observations. The
529 main findings are summarized in Table 4. It should be noted that “ Q ” may refer
530 to different physical quantities depending on the experimental apparatus (torsion
531 versus vibration). Relations between laboratory Q and seismic Q for both P and
532 S waves are carefully examined in Tittmann et al. (1978).

533 In a series of papers (see Table 4), Tittmann and co-workers conclusively
534 demonstrated that the large difference between in-situ seismic measurements and
535 their laboratory counterpart could be ascribed to the adsorption of volatiles at the
536 interface of minerals. In particular, infinitesimal quantities of water reduce the Q
537 dramatically so that contamination by laboratory air suffices to hamper attenua-
538 tion measurements in normal (P, T, humidity) conditions. Tittmann et al. (1975)
539 and Tittmann (1977) showed that intensive degassing by a heating/cool-down
540 treatment dramatically increases the lunar sample Q at both 50Hz and 20kHz.
541 Further analyses conducted in an extreme vacuum demonstrated that the very
542 high Q of lunar rocks may be entirely explained by the absence of volatiles in the
543 crust of the Moon.

544 4.3 Seismic attenuation measurements: an overview of approaches

545 *Methods based on the diffusion model.* Scattering and dissipation convey inde-
546 pendent information on the propagation medium so that it is valuable to try to
547 evaluate separately the contribution of the two mechanisms. The theory of wave
548 propagation in heterogeneous media shows that separation is indeed possible pro-
549 vided one measures the signal intensity at different offsets between source and
550 station and in different time windows (see Sato et al., 2012, for a comprehensive
551 review). Thus, methods based on the diffusion model have the potential to resolve
552 independently the Q and D structure. This may be achieved by direct modeling of
553 the envelope of signals (Dainty et al., 1974) or by fitting the distance dependence
554 of derived quantities such as the maximum amplitude (Nakamura, 1976) or the
555 delay time t_d (Gillet et al., 2017). Because scattering properties depend on the ra-
556 tio between the wavelength and the correlation length of heterogeneities, analyses
557 are most often performed after application of a narrow band-pass filter and shed
558 light on the frequency dependence of the attenuation properties. The neglect of the
559 coherent (or ballistic) propagation, however, is a strong limitation of the diffusion
560 approach. While both diffusivity and seismic Q depend linearly on the individual
561 scattering and absorption properties of P and S waves, diffusion considers the

562 transport of the total, i.e., kinetic and potential, energy only and cannot resolve
 563 the contribution of the different propagation modes. It is worth pointing out that
 564 multiple scattering results in an equipartition of energy among all propagating
 565 modes so that the typical ratio between the S and P energy density is given by
 566 $2(V_p/V_s)^3$. Therefore the Q and D deduced from the diffusion model are mostly
 567 representative of the properties of S waves.

568 *Spectral ratio technique.* Another approach to the measurement of attenuation is
 569 based on the decay of the typical amplitude of direct P - and S -waves as a function
 570 of hypocentral distance. In short-period terrestrial seismology, this is most often
 571 performed by averaging the amplitude in a time window of a few seconds around
 572 the direct arrivals (P or S). The measurement is subsequently corrected for source
 573 and site effect by the coda normalization method (Sato et al., 2012). A linear
 574 regression of the data in the distance–log(amplitude) plane yields an estimate for
 575 Q . In this case only an apparent Q combining effects of scattering and absorption
 576 can be retrieved. The lunar case presents a more complicated case because the
 577 distance between stations is too large to apply coda normalization. As a remedy,
 578 some authors like Nakamura and Koyama (1982) advocate the use of the median
 579 of the amplitudes measured on a set of events to normalize the data. Furthermore,
 580 scattering on the Moon is so strong, particularly in the first tens of kilometers
 581 (see below), that it is necessary to compute the mean amplitude of the P or
 582 S wave train over a long time window (1 or 2 minutes) to average out signal
 583 fluctuations. Intuition suggests that this procedure somehow “corrects” for the
 584 strong broadening of the signal caused by multiple scattering so that it may be
 585 expected that the so-retrieved Q mostly reflects dissipation properties. When few
 586 stations are available, as on the Moon, it is also preferable to use spectral ratios
 587 between pairs of stations (rather than decay with distance) and to perform a
 588 regression of the decay of the amplitude ratio in the frequency domain. In simple
 589 stratified models, the attenuation estimated in this two-station approach may be
 590 ascribed to the depth interval where the rays do not overlap. This method however
 591 implicitly requires that attenuation be frequency independent, which is a severe
 592 limitation. This difficulty has been overcome by Nakamura and Koyama (1982)
 593 who developed a rather sophisticated method employing both single and two-
 594 stations measurements.

595 4.4 Estimates of diffusivity (D) and dissipation (Q).

596 *Results of diffusion modeling.* Latham et al. (1970a,b) fitted seismogram envelopes
 597 with a diffusion model in Cartesian geometry to estimate Q (≈ 3000) and D
 598 ($\approx 2.5 \text{ km}^2/\text{s}$) at 1Hz in the upper crust of the Moon.

599 Dainty et al. (1974) pointed out that the delay time of the maximum t_d seemed
 600 to plateau beyond 170 km distance from the source. They interpreted this obser-
 601 vation as a signature of heterogeneity stratification in the Moon and proposed
 602 that the first ten km of the Moon would be highly scattering while the underlying
 603 medium would be transparent. Based on envelope fitting, they re-evaluated the
 604 diffusivity and Q at two different frequencies (see Table 3). Dainty et al. (1974)
 605 found significantly higher Q than previous authors. They explained the difference
 606 by the fact that part of the decay of the coda originated structurally: the energy

607 that leaks out of the scattering layer is an apparent loss so that the Q estimated
608 from coda decay tends to overestimate effects of dissipation. While the explana-
609 tion of Dainty et al. (1974) is reasonable, their model was designed in Cartesian
610 geometry so that no energy would be able to re-enter the scattering layer.

611 Gillet et al. (2017) has extended this “refraction” of diffuse waves to spherical
612 geometry and showed it to be the key process in explaining the non-monotonous
613 dependence of the delay time t_d on epicentral distance. Using global t_d measure-
614 ments, Gillet et al. (2017) confirmed the existence of a strong stratification of het-
615 erogeneity and found that scattering would be efficient up to a depth of roughly
616 100 km, which would correspond to the base of the mega-regolith. Their analysis
617 showed no evidence for stratification of Q .

618 Nakamura (1976) used the lunar rover as an active seismic source to study
619 the diffusion and dissipation of energy in the uppermost crust of the Moon. This
620 method uses the difference of maximum amplitude for sources approaching or
621 receding from the seismic stations, respectively. He performed observations around
622 4 Hz, 5.6 Hz and 8 Hz to study the frequency dependency of Q and D (see Table 3
623 for details). Within the studied areas, near Apollo stations 15 and 16, no significant
624 regional differences were detected. Although the measurements were not performed
625 in the same frequency band, the values of Q and D reported by Nakamura (1976)
626 are much lower than those found by Gillet et al. (2017). This suggests the existence
627 of a strong depth dependence of D and Q in the first kilometer of the Moon.

628 *Results of the spectral ratio method.* With the exception of the work of Nakamura
629 and Koyama (1982), the spectral ratio method only gives access to an average
630 value of attenuation in a given frequency band. It has the potential, however, to
631 distinguish between Q_p and Q_s and to constrain the attenuation at greater depth
632 than the diffusion method (which is likely limited to the first 150 km of the Moon).
633 An important outcome of attenuation studies based on the spectral ratio approach
634 is that the data require a stratified Q in the mantle.

635 By studying events with different penetration depths, Dainty et al. (1976a)
636 concluded that the upper 500 km has Q_p values as high as 5000 and then decreases
637 with depth. They suggest Q_p values of, respectively, 3500, 1400 and 1100 for the
638 depth intervals 500–600 km, 600–950 km and 950–1200 km. Dainty et al. (1976b)
639 reported similar Q_p values (1400 ± 300 above 520 km depth and 4800 ± 900
640 below), but note that their estimation is not reliable below 1000 km. A similar
641 decrease of Q_p with depth was also reported by Nakamura et al. (1976), who
642 studied the ratio of amplitude variations with epicentral distance at two different
643 frequencies (1 Hz and 8 Hz). Using amplitude variations in the epicentral distance
644 range 40° – 90° , they obtained $Q \approx 4000$, which they regarded as representative
645 of the upper mantle. From the data at 110° – 120° epicentral distance, they found
646 $Q \approx 1500$, confirming the observation that mantle Q_p appears to decrease with
647 depth.

648 Finally, Nakamura and Koyama (1982) used spectra of records from shallow
649 moonquakes from 3Hz to 8Hz to study the frequency dependence of the seismic Q
650 for both P and S waves. They focused on events in the 30° – 90° epicentral distance
651 range, corresponding to rays bottoming in the upper mantle. In spite of large
652 uncertainties regarding geometrical spreading, the results showed that Q_P should
653 be greater than 4000 at 3 Hz and between 4000–8000 at 8 Hz. This frequency
654 dependence, however, is not deemed significant since it resides within error bars.

655 On the other hand, possible values for Q_S are 4000–15000 at 3 Hz and 7000–1500
656 at 8 Hz. This frequency dependence can be considered significant and may be
657 summarized as $Q_S \propto f^{0.7 \pm 0.1}$.

658 **4.5 Future work**

659 In summary, the mantle of the Moon is most probably highly transparent, so that
660 diffusion theory does a poor job at modeling the energy propagation at depth.
661 On the other hand, interpretation of results from the spectral ratio technique
662 is complicated by the coupling of modes that occurs upon scattering. Both the
663 diffusion and spectral ratio technique have merits so that a method that would
664 facilitate the simultaneous analysis of direct and scattered wave trains would be
665 desirable. Radiative transfer (Margerin and Nolet, 2003) or simulations based on
666 the Monte Carlo method (Blanchette-Guertin et al., 2015) are both promising
667 methods.

668 **5 Seismic source locations**

669 To infer a velocity model requires accurate location of all seismic sources. For all
670 naturally occurring events, i.e., meteoroid impacts and shallow and deep moon-
671 quakes, events parameters need to be determined before or with the structural
672 parameters from the lunar seismic arrival time data set. Such inversions, however,
673 can be affected by trade-offs between source location and velocity model. A com-
674 pilation of determined epicentral locations based on both Apollo-era and recent
675 studies are shown in Fig. 6. Errors on locations are generally large, reflecting dis-
676 crepant data analysis and inversion methods. Hempel et al. (2012) also showed
677 that the small-aperture Apollo network limited the accuracy with which many
678 deep moonquake nests could be located (Fig. 7). The characteristics of the various
679 events are discussed in detail in the companion paper (section 3). Here, we only
680 discuss various location estimates.

681 Oberst (1989) obtained the locations of 18 large meteoroid impact events by
682 compiling a set of arrival time measurements based on own work and earlier mea-
683 surements by Goins (1978) and Horvath (1979). The large events were then used
684 as “master events” to establish the relationship between the distances, amplitudes,
685 and rise times of the meteoroid impact signals. Relying on these empirical rela-
686 tionships, locations and magnitudes of 73 smaller meteoroid impacts were estimated
687 by Oberst (1989). Most of the located small events were found to have occurred
688 around the stations. Subsequent reprocessing of the data by Lognonné et al. (2003)
689 resulted in the detection of 19 meteoroid impact events, which were relocated by
690 Garcia et al. (2006) and Garcia et al. (2011) and are shown in Fig. 6b. In the 8
691 years of seismic monitoring, about 1730 impacts were detected (Nakamura et al.,
692 1982).

693 The rarer shallow moonquakes (28 in total, with an average 5 events per year)
694 were first identified as high-frequency teleseismic (HFT) events (Nakamura et al.,
695 1974). Although rare (Nakamura et al., 1976), their large amplitude, strong shear-
696 wave arrival, and unusually high frequency content make these events distinct from

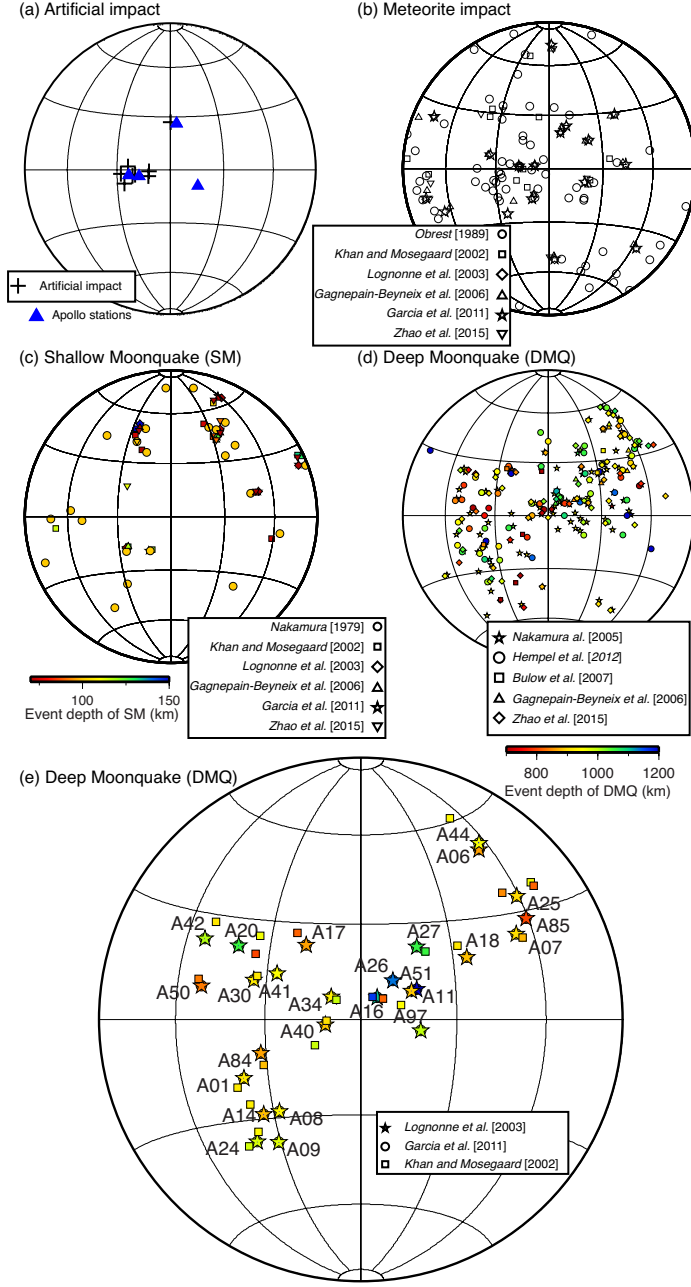


Fig. 6: Locations of impacts and moonquakes on the lunar nearside. The locations of (a) artificial impacts, (b) meteoroid impacts, (c) shallow moonquakes, (d) and (e) deep moonquakes from different studies are displayed. The locations of artificial impacts are from Garcia et al. (2011). The blue triangles in (a) represent the locations of 4 seismic stations. Note that the event depths of shallow moonquakes in Nakamura et al. (1979) were fixed to 100 km. (d)-(e) display the source locations of the DMQ's from different studies. The color denotes event depth. Note the location of Hempel et al. (2012) in (d) is the centroid of location cloud instead of an absolute location, which is resolved in other studies.

the other type of sources. While clearly of internal origin, it has proved challenging to determine source depth from first-arrival time readings. Nakamura et al. (1979) examined the variation of the amplitude with distance, which suggested that the shallow moonquakes occur in the upper mantle of the Moon. Assuming a source depth of 100 km, Nakamura et al. (1979) attempted to establish a possible link between the shallow moonquakes with lunar impact basins. While not conclusive, source depths around 100 km seemed reasonable given the available evidence. Although uncertainties remain large, subsequent arrival time inversions generally confirm this observation with HFT source depths constrained to 50–200 km (Lognonné et al., 2003; Garcia et al., 2006; Garcia et al., 2011; Gagnepain-Beyneix et al., 2006; Khan and Mosegaard, 2002)(Fig. 6c). By modeling the attenuation properties of short-period body waves that are generated by the shallow moonquakes, Gillet et al. (2017) concluded that HFTs are confined to the depth range 50 ± 20 km, which suggests brittle failure of deep faults as possible origin. Frohlich and Nakamura (2006) have also invoked strange quark matter as a possible source of HFTs, based on the observation that essentially all of the 28 shallow moonquakes occurred when the Moon was facing a certain direction relative to stars. This implies that the HFT events could be either caused or triggered by unknown objects that originates extraneous to the solar system.

The most numerous signals recorded by the seismic network were the deep moonquakes (DMQs). A particular feature of the DMQs is that they are clustered in discrete regions (nests). Stacking events from the same nest enhances signal-to-noise ratio and therefore picking accuracy even in the case of small-amplitude seismic signals, as a result of which picks are generally made on stacked DMQ waveforms. Location errors are typically large and different studies show significant discrepancy (Fig. 6d–e and Fig. 7), which reflects differences in underlying assumptions and modeling aspects (Lognonné et al., 2003; Garcia et al., 2011; Gagnepain-Beyneix et al., 2006; Khan and Mosegaard, 2002; Zhao et al., 2015). More details on DMQ analysis and characteristics is provided in our companion paper (Nunn et al., Submitted).

6 Seismic model inversions

In view of the re-compiled Apollo lunar seismic arrival time data set (Nunn et al., Submitted) and the latest a priori assumptions described earlier, we re-assess interior structure. For this purpose, we consider three independent parameterisations and inversion methods. The goal here is not to produce a single model, but rather a family of models that fit the data and are consistent with the most recent set of prior constraints. Although we make the simplifying assumption of keeping source parameters fixed, this approach will allow us to identify similarities and discrepancies among the various internal structure models in order to determine properly resolved structures. We consider three parameterisations and inversions based on the previous work of Drilleau et al. (2013), Garcia et al. (2011), and Khan et al. (2014). These studies span a relatively wide range in terms of model parameterisation from the “standard” seismic parameterisation (model 1), to a simplified equation-of-state method (model 2) over a fully self-consistent thermodynamic method (model 3) that allows for the computation of petrologic phase equilibria and seismic properties. As for the inversions, we consider a two-pronged approach

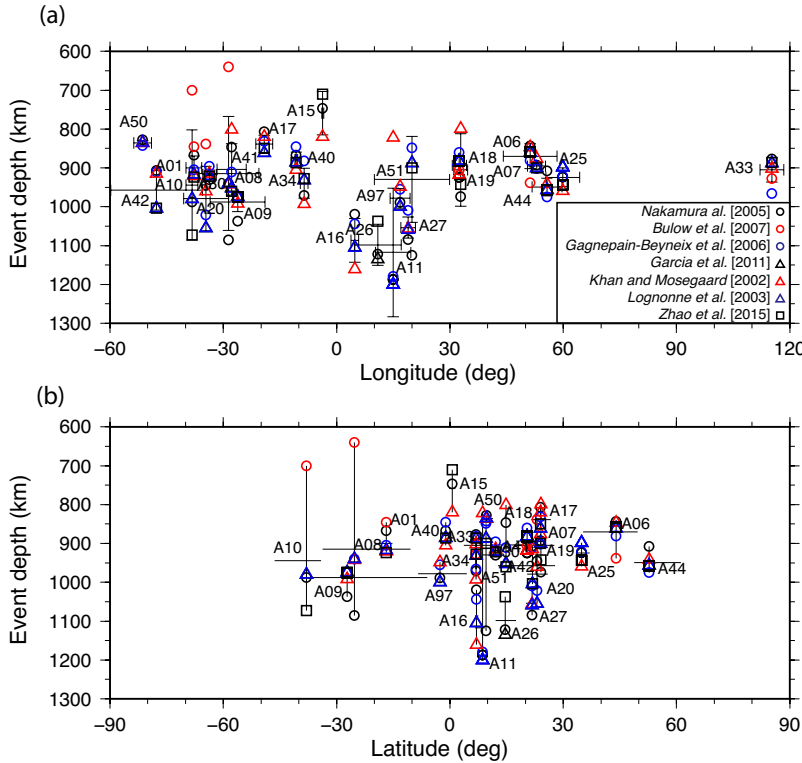


Fig. 7: Variations of the locations of the deep moonquakes (DMQ's) from different studies. (a) displays the mean and standard deviation of DMQ hypocentral coordinates based on different studies (see main text and Fig. 6 for details). (b) displays the mean and range of DMQ locations. Only DMQ clusters for which at least three studies provide locations are plotted here. To emphasize the depth variation, individual DMQ locations from different studies are plotted using different symbols with varied depths using same (a) mean longitude and (b) mean latitude.

743 that involves both model inversion (models 1 and 2) and model assessment (model
 744 3). Models based on parameterisations 1 and 2 are obtained from inversion of the
 745 lunar seismic travel time data set, whereas models relying on parameterisation 3
 746 are only used in a predictive sense, i.e., models obtained from inversion of electro-
 747 magnetic sounding (Table 6) and geodetic data (k_2 , M , and I/MR^2) are employed
 748 to predict P- and S-wave travel times that are subsequently compared to obser-
 749 vations. While the fit to the travel time data for this particular set of models will
 750 evidently be less than for the other models, this predictive exercise is neverthe-
 751 less important as it assesses to 1) what extent the different geophysical data sets
 752 are compatible; 2) the reliability of the underlying parameterisation to simulta-
 753 neously fit geophysical data sets that are sensitive to distinct physical properties
 754 (e.g., seismic wave speeds, density, electrical conductivity). The forward modeling
 755 scheme, i.e., mapping from model structure to travel times, relies in all three cases

on a ray-theoretical approach to compute body wave travel times. The specific data used in the inversion are the median P and S arrival times compiled in our companion paper for M1 and M2, and the latest geodetic observations (k_2, h_2, M , and I/MR^2) (for $\alpha=0.3$) compiled in Table 5 for M2 and M3, with the simplifying assumption that the solid-body mean moment of inertia (I_s) is equal to that of the entire body. Common to all three models are assumptions of a spherically symmetric body.

6.1 Model parameterisation and prior information

6.1.1 Model 1

The models are parameterized with Bézier points, which are interpolated using polynomial C_1 Bézier curves. The advantages of this parameterisation is that it relies on a small number of parameters (Bézier points) and it does not impose a regularly spaced discretization of the models or prior constraints on layer thicknesses and location of seismic discontinuities. It can be used to describe both a gradient and a sharp interface with a minimum of parameters (the reader is referred to Drilleau et al. (2013) for more details). The inverted parameters are the 2 vectors corresponding to the Bézier points for V_P , and the depth at which these Bézier points are located. The Bézier points are randomly located in depth within the prior range (see Table 8). The model parameter vector contains 15 points with the last point located at the core-mantle-boundary (CMB). The depth to the CMB is allowed to vary between 1200 and 1400 km depth. In order to estimate V_S , the V_P/V_S ratio profile is also inverted for using 4 Bézier points that are randomly sampled between 1.5 and 2.2. Note that density is not inverted for with this approach. For the core, we assume that it is entirely liquid and homogeneous, as a consequence of which $V_S = 0$ km/s and V_P is randomly sampled between 0.5 and 9.5 km/s. To account for local differences beneath stations, P - and S -wave station corrections are considered by adding to the computed P - and S -wave travel times, for a given model, a value randomly sampled between -4 and 4 s.

To compute body wave travel times, we rely on the ray tracing algorithm of Shearer (2009). To solve the inverse problem, we employ a Markov chain Monte Carlo approach (Mosegaard and Tarantola, 1995). This technique allows us to sample a large range of models and provides a quantitative measure of model uncertainty and non-uniqueness. Prior information on model parameters is summarised in Table 8.

6.1.2 Model 2

This parameterisation is an improved version of the parameterisation used by Garcia et al. (2011). The crust is fixed in terms of velocity and density, but the average crustal thickness is a free parameter. The seismic/density model of the mantle is separated into two parts: a lithosphere which covers the region from the crust-mantle boundary to radius R_L in which the thermal gradient ($(\frac{dT}{dz})_{OA}$) is assumed to be constant, and an adiabatic part from radius R_L to the CMB (radius R_{CMB}).

798 In the lithosphere, the seismic/density model follows the modified Adams-
 799 Williamson equation (Stacey and Davis, 2008) :

$$\frac{d\rho}{dz} = \frac{\rho g}{\phi} - \alpha \rho \tau \quad (1)$$

800 where ρ is density, z is depth, g is gravitational acceleration, $\phi = \frac{K_T}{\rho} = V_P^2 - \frac{4}{3}V_S^2$
 801 the seismic parameter, K_T is incompressibility, α is thermal expansion and τ is
 802 the super adiabatic gradient. This last term is defined by the following equation:

$$\tau = \frac{dT}{dz} - \left(\frac{dT}{dz} \right)_{adiabatic} = \left(\frac{dT}{dz} \right)_{OA} \quad (2)$$

803 in which the adiabatic gradient is defined by : $\left(\frac{dT}{dz} \right)_{adiabatic} = -\frac{g}{\alpha \phi}$.

804 The Adams-Williamson equation assumes an adiabatic gradient, and conse-
 805 quently, $\tau = 0$. Given lunar mass, or equivalently surface gravity acceleration, and
 806 the seismic velocity model, the Adams-Williamson equation is integrated from top
 807 to bottom to compute density. To compute V_P from the density model, we employ
 808 Birch's law with constant parameters (a and b) over the mantle. The $\frac{V_P}{V_S}$ ratio
 809 profile is inverted with three reference points at the top and bottom of the mantle
 810 and at 700 km radius. This parameter is linearly interpolated in between these
 811 reference points and used to determine V_S .

812 However, in the lithosphere where thermal gradients are likely super adiabatic,
 813 the integration of equation (1) requires the knowledge of both τ and α . Our model
 814 parameterisation assumes that $\tau = \left(\frac{dT}{dz} \right)_{OA}$ is constant in the lithosphere. How-
 815 ever, thermal expansion α varies with pressure, temperature, and density. We take
 816 two important assumptions. First we assume that the product $\alpha \cdot K_T$ is constant
 817 over the whole mantle and equal to $4.0 \cdot 10^6 \pm 0.8 \cdot 10^6 \text{ MPa/K}$ (Stixrude and
 818 Lithgow-Bertelloni, 2005). Next, we assume that the gruneisen parameter is also
 819 constant for the whole mantle and equal to $\gamma_{th} = 1.2 \pm 0.2$ (Poirier, 2000). Fi-
 820 nally, knowing seismic velocities, and consequently the adiabatic incompressibility
 821 K_S and temperature, we can use a set of well-known thermodynamic relations to
 822 estimate α through the following relation (Poirier, 2000):

$$\alpha = \frac{(\alpha K_T)}{K_S - \gamma_{th} \cdot (\alpha K_T) \cdot T} \quad (3)$$

823 where T is temperature. This formulation imposes the computation of the absolute
 824 temperature, whereas up to now only temperature gradients in the mantle were
 825 needed. To scale our mantle temperature model we will assume arbitrarily that
 826 the temperature at the crust-mantle boundary is equal to 300 K. Error analysis
 827 suggests that the error on α so estimated is dominated by the error of the product
 828 $\alpha \cdot K_T$ (20%) even in the case of large errors (~ 300 K) on absolute temperatures.
 829 Once thermal expansion has been computed, equation (1) can be integrated with
 830 Birch's law and $\frac{V_P}{V_S}$ ratio to construct seismic and thermal profiles of the litho-
 831 sphere. The same method is applied to the adiabatic part at the bottom of the
 832 mantle with $\tau = 0.0$. The core is parameterized using an average radius and den-
 833 sity. Constant values for P and S wave velocities are fixed to 4.0 km/s and 0.0
 834 km/s, respectively, to allow for the computation of Love numbers. The effect of
 835 core properties have little influence on the Love numbers because of the small size

836 of the core. Core density will be deduced from the rest of the model parameters
 837 by fitting lunar mass and moment of inertia.

838 Model parameters are summarized in Table 9. The inversion is performed by
 839 building lunar models (seismic velocity and density profiles) from random values
 840 of the inverted parameters. Then, only lunar models predicting geodetic variables
 841 within their error bars are selected (see Table 5). A first set of 30 lunar models for
 842 each core radii (sampled by 5 km steps from 250 to 550 km radius) are selected. For
 843 each of these models station correction parameters (T_{corP} and T_{corS}) are inverted
 844 to minimize the cost function of seismic travel times. Then, the parameter space
 845 is explored using the Neighbourhood Algorithm (Sambridge, 1999) at each core
 846 radius, always imposing that the selected models predict geodetic variables within
 847 their error bars, and inverting for station correction parameters. The Neighbour-
 848 hood Algorithm is performed with 16 loops exploring the neighbourhood of the
 849 3 best models of the parameter space with 10 new models. The whole ensemble
 850 of models explored is considered, and only 1% of the models with the best cost
 851 function are kept for the ensemble analysis.

852 6.1.3 Model 3

853 The composition of the lunar mantle is investigated using the model chemical sys-
 854 tem CaO-FeO-MgO-Al₂O₃-SiO₂-TiO₂ (CFMASTi). We assume that mantle min-
 855 eralogy is dictated by equilibrium and compute this from thermodynamic data as
 856 a function of pressure, temperature, and bulk composition by Gibbs energy min-
 857 imization (Connolly, 2009). For these calculations, we consider the stoichiometric
 858 solid phases and species in the thermodynamic data compilation of Holland and
 859 Powell (1998, revised 2002) together with the silicate melt and non-stoichiometric
 860 phases summarized in Table 2 of Khan et al. (2014). The silicate melt model is
 861 based on pMELTS (Ghiorso et al., 2002). Thermodynamic properties are computed
 862 for the aggregate at the temperature of interest. To determine elastic moduli the
 863 Hashin-Shtrikman bounds are averaged.

864 For this particular model, we assume that the Moon is divided into a num-
 865 ber of layers that constitute crust, upper and lower mantle, and core. Crustal
 866 composition (X_1) is fixed to that of Taylor et al. (2006) and constant thickness
 867 d_1 . To better capture variations in crustal properties (ρ , P - and S -wave speed),
 868 we employ a function of the form $f'_i = f_i \cdot \phi$, where f_i is one of the aforemen-
 869 tioned physical properties in crustal layer i computed thermodynamically and ϕ is
 870 a depth-dependent porosity parameter based on the results from GRAIL (Wiec-
 871 zorek et al., 2013). The mantle is divided into two layers that are parameterized
 872 by thicknesses d_2 and d_3 , compositions X_2 and X_3 and temperature T . Mantle
 873 compositions are uniform in each layer and temperature is defined at a number of
 874 fixed radial nodes. The physical properties of the core are specified by radius (r_c),
 875 density (ρ_c), and electrical conductivity (σ_c), respectively. Model parameterisation
 876 is illustrated in Fig. 8 and prior information is summarised in Table 10.

877 Once all the model parameters values have been assigned, we can compute
 878 radial profiles of equilibrium modal mineralogy, seismic properties, and electrical
 879 conductivity as a function of pressure, temperature, and composition at intervals
 880 of 20 km (thermodynamic nodes) from the surface to the core-mantle-boundary.
 881 Since electrical conductivity is less important in the context of computing seismic

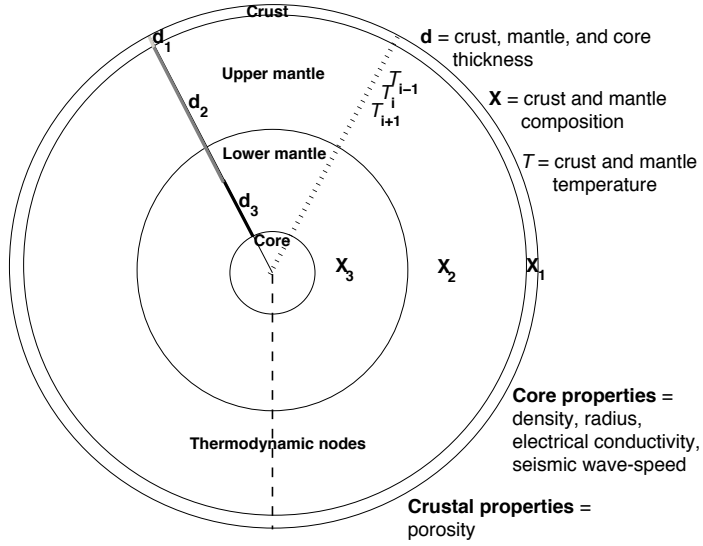


Fig. 8: Model 3 parameterisation.

882 travel times, we skip the details of how bulk electrical conductivity profiles (shown
 883 in Fig. 2a) are determined and refer the interested reader to Khan et al. (2014).

884 6.2 Definition of cost function

885 We use the following L₁ norm-based cost function

$$J_1 = \sum_{N_p} \frac{|T_p^{obs} - T_p^{calc}|}{\sigma_p} \sum_{N_s} \frac{|T_s^{obs} - T_s^{calc}|}{\sigma_s} \quad (4)$$

$$J_2 = \frac{|M^{obs} - M^{calc}|}{\sigma_M} + \frac{|C^{obs} - C^{calc}|}{\sigma_c} \quad (5)$$

$$J_3 = \frac{|k_2^{obs} - k_2^{calc}|}{\sigma_{k_2}} + \frac{|h_2^{obs} - h_2^{calc}|}{\sigma_{h_2}} \quad (6)$$

$$J_4 = \sum_{\omega} \frac{|\rho_a^{obs}(\omega) - \rho_a^{calc}(\omega)|}{\sigma_{\rho_a}} \quad (7)$$

886 where the first cost function (J_1) computes the misfit between the number of ob-
 887 served (N_p , N_s) and computed P (T_p) and S (T_s) wave travel times within error
 888 bars (σ_p and σ_s) (see Fig. 11 of Nunn et al., Submitted). The second and third
 889 cost functions (J_2 and J_3) determine fits to mean mass (M) and mean moment
 890 of inertia ($C = I/MR^2$), degree-2 Love numbers determining gravity (k_2) and
 891 shape (h_2) responses, respectively, within error bars σ_k , where k refers to either
 892 M , I/MR^2 , k_2 or h_2 (Table 5). The fourth cost function (J_4) determines the fit to
 893 electromagnetic sounding data within errors σ_{ρ_a} (Table 6). Superscripts through-
 894 out refer to observations (obs) and computed data (calc). Due to the differing
 895

model parameterisations, model suite 1 (M1) only minimizes J_1 , whereas model suite 2 (M2) minimizes $J_1 + J_2 + J_3$ and model suite 3 (M3) minimizes $J_2 + J_3 + J_4$ while computing J_1 in a predictive sense. Inversion output consists of ensembles of internal structure models that fit the cost functions.

6.3 Inversion results and discussion

Results from the inversions in the form of median profiles of V_P , V_S , and ρ , including mean absolute deviation, are shown in Fig. 9. For comparison, some recent models discussed in section 3 are also shown. For further use, median models are compiled in Appendix .1 and Table 11. Misfit values and computed P- and S-wave travel times for the three models are shown in Fig. 10 and 11, respectively.

By comparing the three models, the following observations can be made:

1. Crustal structure differs between the three models and reflects the different prior constraints employed: M1: variable crustal thickness without imposing a crust-mantle discontinuity; M2: variable crustal thickness with an imposed crust-mantle discontinuity; and M3: fixed crust-mantle discontinuity at 40 km depth.
2. In the uppermost mantle (depth range 60–200 km), models M1 and M2 are in good agreement and suggest the presence of a low-velocity layer (LVL). The extent of this layer differs between the two models, which possibly relates to their different crustal structures. An indication of the presence of a LVL in the upper mantle was first noted from the difference in arrival times from shallow moonquakes compared with those from deep moonquakes and meteoroid impacts (Nakamura et al., 1974). Khan et al. (2006a) also found a decrease in V_S with depth owing to the enhanced effect of temperature on V_S over that of pressure. There is less overlap between M1 and M2 in the mid-mantle (depth range 200–500 km). Model M3 differs throughout this depth range with significantly higher seismic P-wave speeds but moderately overlapping S-wave speeds (in the depth range 100–250 km). These differences between M1/M2 and M3 are also discernable from the travel time residuals plotted in Fig. 11, where a positive trend for P-waves in the 25°–80° epicentral distance range is apparent for M3, but less so for M1 and M2. This difference between M1/M2 and M3 suggests that the seismic data constrain the first 600 km of the lunar interior.
3. In the mid-to-lower mantle (depth range 600–1200 km), the seismic profiles for all three models generally overlap over the entire range, indicative of a relatively uniform lower mantle with no clear evidence for a mid-mantle discontinuity as suggested in earlier studies (Nakamura, 1983; Khan and Mosegaard, 2002). Both the model based only on seismological data (M1) and the one relying on mineral physics assumption (M3) agree on that point.
4. Below ~1200 km depth model variability increases for all three models and indicates the maximum depth to which the seismic wave speeds are properly constrained by the seismic travel time data set.
5. A relatively strong decrease in seismic wave speed at the base of the mantle is apparent in M1 and M3. In the case of M1 and M2, this velocity decrease is driven by having to fit strongly positive residual P- and S-wave travel times at large epicentral distances, whereas for M3 a "soft" zone is required to explain the Love number. While geophysical evidence for partial melt in the deep

944 lunar interior is accumulating (Nakamura et al., 1973; Williams et al., 2001a;
945 Efroimsky, 2012b,a; Khan et al., 2014; Harada et al., 2014), models using
946 different rheologies are also able to reproduce the geophysical observations
947 (Nimmo et al., 2012).

- 948 7. While the models are capable of fitting the P wave arrivals at large epicentral
949 distances, none of them are able to fit the strongly delayed S-wave travel times
950 (Fig. 11), even in the case of models M1 and M3, that contain very low S-wave
951 velocities at the base of the mantle. Because these travel times emanate from a
952 single farside meteoroid impact and a farside deep moonquake, it suggests that
953 the S-wave arrival time readings for these particular events are wrongly picked
954 in the coda because the otherwise abrupt S-wave arrival has been attenuated. A
955 possible explanation for this, includes either a lower mantle with a partial melt
956 layer, which would strongly attenuate S-waves and create a shadow zone so as
957 to render these difficult to observe or, alternatively, a large core that diffracts P-
958 waves and produces arrivals at large distances, while the amplitude of diffracted
959 S-waves decreases quickly with distance and provide an explanation for the
960 absence of clear S-wave arrivals at large distances. These effects are illustrated
961 in Fig. 12, which shows ray paths for S-waves in a model with (M1) and without
962 (M2) a lower mantle low-velocity layer. A shadow zone is clearly present in the
963 case of M1, whereas the effects of diffracted waves are seen in the case of M2.
964 8. Only model suites M2 and M3 are capable of constraining density structure.
965 As in the case of seismic wave speeds, M3 is denser than M2 over most of the
966 upper and mid-mantle. While the M2 distribution in the core region is wider
967 than M3, densities overlap and suggest average core densities in the range 4–5
968 g/cm³. Densities in this range are incompatible with a pure Fe core, but suggest
969 a small core (~350 km in radius) consisting of Fe with a substantial amount
970 of light elements (Fig. 3b). From the data considered here, it is not possible to
971 resolve an inner core since neither density nor absolute P-wave speed are well
972 constrained in this region.

973 L₁-based misfit values for the three inversions are shown in Fig. 10. As ex-
974 pected, models M3 misfit values are significantly higher than both M2 and M1
975 given that models M3 are not obtained by inversion of the seismic travel time
976 data. Despite different parameterizations and different crustal structure, models
977 M1 and M2 produce similar misfit values with the more flexible parameterization
978 of M1 resulting in the lowest misfit values. Based on this, we can make the follow-
979 ing observations: 1) a seismic discontinuity separating crust and upper mantle is
980 not necessarily required by the travel time data, although it should be noted that
981 there are other arguments based on the seismic data that favour a discontinuity,
982 e.g., crust-mantle body wave conversions and amplitude considerations, (Vinnik
983 et al., 2001; Khan and Mosegaard, 2002); 2) that uncertainties on the Apollo seis-
984 mic travel time readings allow for a relatively large model spread; and 3) core size
985 and composition (density) continue to remain elusive due to the general scarcity
986 of data that directly sense the core and, not least, a lunar moment of inertia that
987 is almost equal to that of a homogeneous sphere. Nevertheless, current consensus
988 (Table 1) suggests a core 350±40 km in radius with an Fe-like composition.

989 To better model lateral heterogeneities beneath stations, P- and S-wave sta-
990 tion corrections have been applied to all travel times. The average P- and S-wave
991 correction is set zero to avoid biasing velocity model estimates. Fig. 13 summarises

992 the inverted station corrections. These are broadly distributed for M1 and more
993 peaked for the M2 models that invoke stronger prior constraints (note that M3
994 does not use station corrections). The consistency between the corrections of the
995 different models is not ensured for all stations nor is its sign, i.e., whether posi-
996 tive or negative. These observations suggest that the station corrections are likely
997 absorbing a number of effects including lateral heterogeneities between stations,
998 variations of these heterogeneities with incidence angle, event mislocations and
999 any other instrument or site effect at a given station. The variations of these pa-
1000 rameters between M1 and M2 inversions and for the different velocity models of a
1001 given inversion suggest that these estimates are correlated to the inverted velocity
1002 model.

1003 The low velocity layer at the top of the mantle is interpreted in terms of over-
1004 adiabatic thermal gradient. To do so, the excess thermal gradient relative to the
1005 adiabatic gradient as a function of lithosphere thickness are shown for the 1%
1006 best models of M2 in Fig. 14. The distribution clearly shows two types of models:
1007 models with thick lithospheres and low values of over-adiabatic thermal gradients,
1008 and models with thin lithospheres and large over-adiabatic thermal gradients.
1009 The low velocity layer is driven by this second set of models, among which the
1010 best models parameters correspond to an over-adiabatic thermal gradient value
1011 of $0.7 \pm 0.4^{\circ}\text{C}/\text{km}$, translating into a thermal gradient of about $1.7 \pm 0.4^{\circ}\text{C}/\text{km}$,
1012 in a lithosphere extending down to 260 km depth (1425 km radius). This value
1013 is slightly larger than the $\approx 1.3^{\circ}\text{C}/\text{km}$ temperature gradient estimates by Khan
1014 et al. (2006a) and Kuskov and Kronrod (1998), the only studies presenting a
1015 similar upper mantle low velocity layer. Moreover, these values are close to the
1016 value of about $1.4^{\circ}\text{C}/\text{km}$ obtained by Laneuville et al. (2013) for the region below
1017 Procellarum KREEP Terrane (PKT) where the Apollo seismic network is mainly
1018 located. This overall agreement suggests that the low velocity layer observed by
1019 Apollo seismic network may be linked to the presence of the PKT region.

1020 7 Conclusion and outlook

1021 In this study, we have provided an overview of lunar seismicity, internal structure
1022 models, including scattering and attenuation properties of crust and mantle, lunar
1023 geophysical data sets other than the seismic data, and information pertinent to
1024 the lunar interior from modeling studies and laboratory measurements.

1025 The comparison between the various seismic wave speed and attenuation mod-
1026 els shows similarities and discrepancies. For example, crustal thickness in the vicin-
1027 ity of Apollo stations 12 and 14 appears to be constrained to within 10 km with a
1028 currently favoured thickness of between 30–40 km. Since a significant part of the
1029 seismic data illuminate upper and mid-mantle, models tend to overlap most in this
1030 particular region. Deep mantle and core structure are poorly constrained mainly
1031 due to the lack of seismic data at large epicentral distances. However, the models
1032 of seismic attenuation and scattering appear to present a relatively consistent pic-
1033 ture in which the intrinsic attenuation inside the Moon is very low ($Q > 1500$) at
1034 all depths, and scattering is dominated by fracturing in the crust and upper man-
1035 tle down to ~ 100 km depth. In summary, large uncertainties persist and future
1036 studies relying on expanded and improved data will have to refine present results.

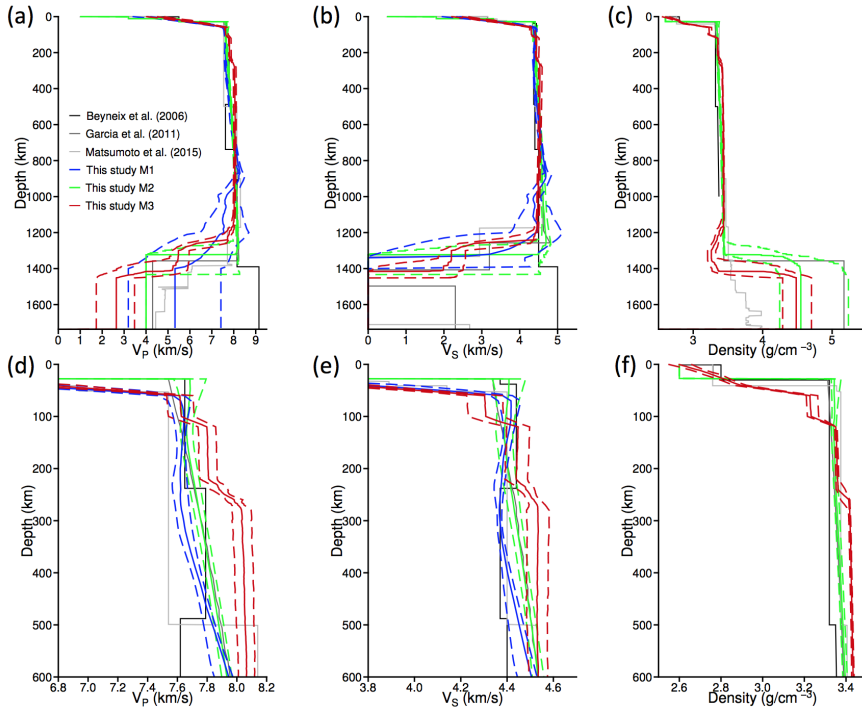


Fig. 9: Comparison of previously published lunar internal structure models with model suites M1, M2, and M3. Radial profiles of P-wave velocity (a), and S-wave velocity (b), and density (c) as a function of depth. Plots in the bottom panel (d–f) show a zoom on upper mantle structure. Solid and dashed lines show median profiles \pm mean absolute deviation obtained from all sampled models.

As part of this re-assessment, we also performed an inversion of the “new” body wave travel time data presented in our companion paper (Nunn et al., Submitted) as a first step toward a unified reference model of the lunar interior. Three very different model parameterisations were used of which two of the investigated models considered geodetic and electromagnetic sounding data. Comparison between model outputs suggests that, despite large error bars on the arrival time data set, the first 600 km of the lunar interior appears to be relatively consistent between the models with evidence for a low-velocity zone in the 100–250 km depth range. The observed velocity decrease corresponds to a thermal gradient ($\sim 1.7^\circ \text{C/km}$), consistent with previous investigations (Khan et al., 2006a; Kuskov and Kronrod, 1998), and could possibly be linked to the thermal structure (high abundance of heat-producing elements) below the lunar nearside region known as the Procellarum KREEP Terrane (Laneuville et al., 2013).

As a caveat, we should note that our model inversions were performed under the assumption of perfectly known event locations. This is a rather strong assumption, which was invoked for the purpose of comparing different interior structure parameterisations. Clearly, this assumption needs to be relaxed in future applica-

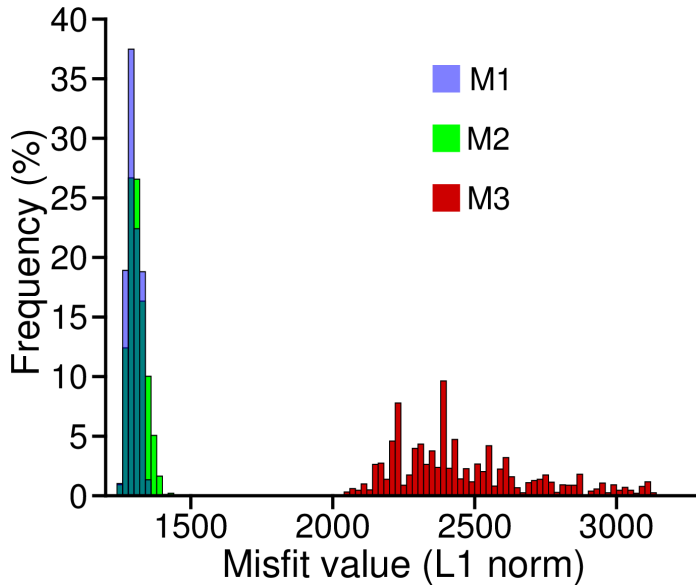


Fig. 10: Distributions of misfit (L_1) values for model suites M1, M2, and M3. Misfit values are based on the “seismic” cost function J_1 (Eq. 4). Model parameterisations are described in section 6.1.

1054 tions given the inherent trade-off between event locations and interior structure.
 1055 Deep moonquake locations, in particular, are strongly model dependent.

1056 Finally, analysis of the lunar seismic data will continue to improve our knowl-
 1057 edge of the lunar interior, although significant improvement in our understanding
 1058 will probably have to await the return of a new set of high-quality seismic data.
 1059 Preferably, these data should be acquired from a spatially and temporally ex-
 1060 tended network of large-bandwidth stations to address some of the outstanding
 1061 issues, such as crustal structure and layering, mantle discontinuities, lateral vari-
 1062 ations and mantle heterogeneities, and core size and composition. To ensure that
 1063 high-quality instruments can be operated simultaneously, a set of low-level require-
 1064 ments have been produced by our team that are described in our companion paper
 1065 (Nunn et al., Submitted).

1066 **Acknowledgements** We acknowledge ISSI Bern and ISSI Beijing for providing support
 1067 to our international research team. This work was granted access to the HPC resources
 1068 of CINES under the allocation A0050407341 made by GENCI. Internal structure models
 1069 and quake locations presented in this study are available in electronic form at the following
 1070 DOI:10.5281/zenodo.3372489.

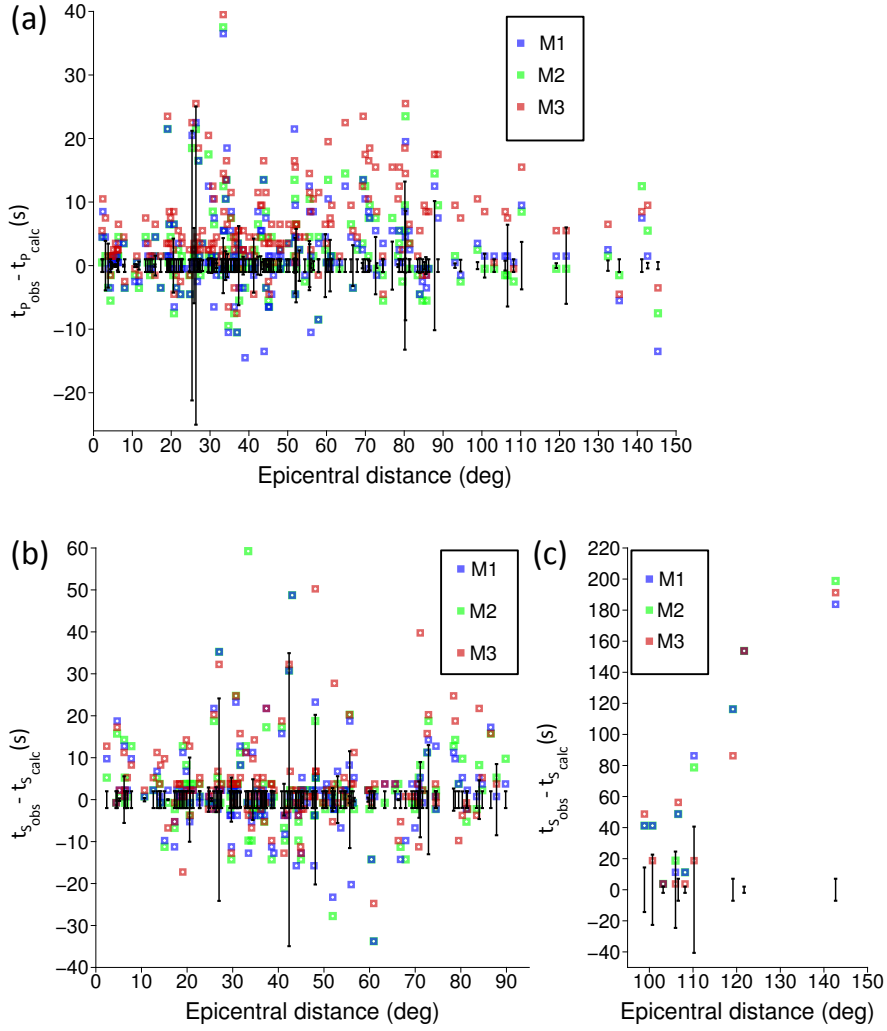


Fig. 11: Differences between observed and computed travel times as a function of epicentral distance for (a) P waves and (b)–(c) S waves. Vertical black lines indicate uncertainties on observed P wave and S wave travel times. M1, M2, and M3 results are shown in blue, green and red, respectively. The computed travel times shown here are for the maximum a posteriori model for each of the model suites M1, M2, and M3.

Model	TK74	NK83	KM02	LG03	BN06	WB11	GR11	KH14	MS15	Best estimate
Data / prior										
Body wave travel times	P only multiple	P+S NK83	P+S own+VK01	P+S+Smpl LG03+VK01	S only own	P + S LG03	None	P + S LG03	P + S NU19	ISSI team H83
EM sounding	None	None	None	None	None	None	H83	None	None	
prior source locations	KV73ab	None	None	None	LG03	LG03	None	LG03	LG03	ISSI team this paper
Mass ($\times 10^{22}$ kg)	None	None	None	None	7.3458	7.3463	7.34630	7.34630	7.34630	
I/MR^2	None	None	None	None	None	0.3932	0.393112	0.393112	0.393112	± 0.00088
k_2	None	None	None	None	0.0213	0.0232	0.02422	0.02422	0.02422	± 0.00012
h_2	None	None	None	None	0.039	None	None	None	0.048	± 0.00058
prior crust seismic model	None	None	None	None	0.008	None	None	None	None	(elastic)
prior crust density	None	None	None	None	LG03	LG03	None	None	None	± 0.006

Table 2: Summary of data sets and prior information of previously published lunar models. Models are named as follows: TK74 == Toksoz et al. (1974), NK83 == Nakamura (1983), KM02 == Khan and Mosegaard (2002), LG03 == Lognonné et al. (2003), BN06 == Gagnepain-Beyneix et al. (2006), WB11 == Weber et al. (2011), GR11 == Garcia et al. (2011), KH14 == Khan et al. (2014) and MS15 == Matsumoto et al. (2015) NU19 == Nunn et al. (Submitted). References cited in the Table are the following: KV73ab == Kovach and Watkins (1973a,b), H83 == Hobbs et al. (1983), VK01 == Vinnik et al. (2001).

Reference	Freq. (Hz)	Freq. Dep.	Depth Range (km)	D (km^2/s)	Q_p	Dissipation Q_s	Observable	Method
Latham et al. (1970a)	1	Yes	< 20	2.3–2.5		3600	Seismogram envelope	Diffusion theory
Latham et al. (1970b)	1	Yes	< 20			3000	Coda Decay	Diffusion theory?
Dainty et al. (1974)	0.45	Yes	< 25	$\parallel 8 \perp 2$		5000	Seismogram Envelope	Diffusion Theory
Dainty et al. (1976a)	1	< 14	< 14	$\parallel 0.9 \perp 0.4$		5000		
Dainty et al. (1976a)	1 – 10	No	0 – 500				Average P-wave amplitude	Inter-station spectral ratio
Dainty et al. (1976b)	1 – 10	No	500 – 600	3500				
Dainty et al. (1976b)	1 – 10	No	600 – 950	1400				
Dainty et al. (1976b)	1 – 10	No	950 – 1200	1100				
Nakamura et al. (1976)	1 – 8	No	< 50	4800 \pm 900			Average P-wave amplitude	Inter-station spectral ratio
Nakamura et al. (1976)	1 – 8	No	520 – 1000	1400 \pm 300				
Nakamura (1976)	4		60 – 300	4000			Average P-wave amplitude	Inter-station spectral ratio
Nakamura (1976)	5.6		300 – 800	1500				
Nakamura (1976)	8		< 2	2.6 \times 10 ⁻² , 3.3 \times 10 ⁻²	1600 – 1700	Maximum amplitude decay	Average P-wave amplitude	Inter-station spectral ratio
Nakamura and Koyama (1982)	1	Yes	< 400	2.2 \times 10 ⁻² , 2.8 \times 10 ⁻²	1900 – 2000	with distance		Diffusion theory for moving sources
Nakamura and Koyama (1982)	8	$Q_s \propto f^{0.7 \pm 1}$		1.8 \times 10 ⁻² , 2.2 \times 10 ⁻²	2300			
Gillet et al. (2017)	0.5	Yes	0 – 61	> 4000	4000 – 150000	Average P, S amplitude	Single + Inter-station Spectral fitting	
Gillet et al. (2017)	0.5	Yes	61 – 95	4000 – 8000	7000 – 150000			Diffusion theory
Gillet et al. (2017)	0.5	Yes	95 – 113	2500 \pm 25				
Gillet et al. (2017)	0.5	Yes	113 – 147	Id.				
Gillet et al. (2017)	0.5	Yes	> 147	365 \pm 150 – 1000 \pm 600	Id.	Rise time and coda Q of seismogram envelope		
Gillet et al. (2017)	0.5	Yes		4585 \pm 2000	Id.			

Table 3: Summary of seismic attenuation estimates in the Moon. The notations \parallel and \perp refer to horizontal and vertical diffusivities, respectively. Frequency Dependence (Freq. Dep.) indicates whether the underlying physical model assumes attenuation to be frequency dependent or not. In the study of Nakamura (1976), the first and second value of D refer to the sites of Apollo 15 and Apollo 16, respectively.

Reference	Mission	Sample Codes	$Q_{F,y}$	$Q_{s,t}$	Method	Environment	Pressure	Temperature	Frequency	Remarks
Kanamori et al. (1970)	Apollo 11	10020/10057/10065	10	10	Amplitude ratio with controlled specimen	Vacuum	200 MPa	Room T.	1 MHz	"At high pressures all the samples... showed an appreciable increase in Q"
Wang et al. (1971)	Apollo 12	12002154/120222, 60	15	17-35	Amplitude ratio with controlled specimen	Air	$F \approx 0$	Room T.	1 MHz	Samples were dried in 100 degrees oven under vacuum for 2 hours
Warren et al. (1971)	Apollo12	12063/12038	130-300		Torsion pendulum	Vacuum	Room P.	Room T.	≈ 1 Hz	"Humidity variation (0-100%) varies Q by factor of 2" "Temperature variation (25°C to 125°C do not change the Q significantly"
Tittmann et al. (1972)	Apollo14	14310,86	10	50-90	Resonance Peak Half-Width	Dry Nitrogen	≈ 0.1 MPa	25°-125°C	40-130 kHz	"Temperature variation from 25°C to 125°C No difference between N2 and vacuum "At higher vacuum and lower temperature, Q value increases and approaches what was observed on the Moon"
Tittmann et al. (1975)	?	70215,85	60	340	Resonance Peak Half-Width	Hot Water Vapor Humid/dry air Vacuum	Room P. Room P. $8e-6$ Pa	Room T. Room T. Room T. -180°C	tens of KHz?	"Showed that Q rapidly decreases with water intrusion." "At higher vacuum and lower temperature, Q value increases and approaches what was observed on the Moon"
Tittmann et al. (1976)	?	70215,85		400		Lab. air Vacuum	$\approx 1.3 \times 10^{-1}$ Pa	Room P.	20 KHz	After 1 st heating+slow cooling
				800		Vacuum	$\approx 1.3 \times 10^{-1}$ Pa	Room T.	20 KHz	After 3 rd heating+rapid cooling
				2420		Vacuum	$\approx 1.3 \times 10^{-4}$ Pa	Room T.	20 KHz	After 4 th heating+rapid cooling
				3130		Vacuum	$\approx 1.3 \times 10^{-5}$ Pa	Room T.	20 KHz	After continued pumping
Tittmann et al. (1977)	?	70215,85			Resonance Peak Half-Width	Vacuum	$\approx 1.3 \times 10^{-5}$ Pa	Room T.	20 KHz	12 Hrs exposition in vacuum
Tittmann (1977)	?	70215,85		4882	Resonance Peak Half-Width	Vacuum	$\approx 1.3 \times 10^{-6}$ Pa	Room T.	20 KHz	12 Hrs exposition in vacuum
						Vacuum	$\approx 1.3 \times 10^{-8}$ Pa	Room T.	20 KHz	14 Hrs exposition in vacuum
Tittmann et al. (1978)	?	70215,85	740	950	Resonance Peak Half-Width	Vacuum	$\approx 7 \times 10^{-8}$ Pa	Room T.	20 KHz	All measurements performed after outgassing
				1330						
				1430						

Table 4: Summary of laboratory measurements of dissipation in Lunar rock samples.

Table 5: Summary of lunar geodetic data parameters and uncertainties used in the inversions.

Variable	Value	Source
Mass	$7.34630 \pm 0.00088 \times 10^{22}$ kg	(Williams et al., 2014)
R	1737.151 km (1737.151 km)	(Wieczorek, 2015)
I_s/MR^2	0.393112 ± 0.000012	(Williams and Boggs, 2015)
k_2 : elastic, $\alpha = 0.3$	0.02294 ± 0.00018	section 2.1 this study
k_2 : elastic, $\alpha = 0.1 - 0.4$	0.02248 ± 0.00072	section 2.1 this study
h_2 (LLR): elastic, $\alpha = 0.3$	0.0450 ± 0.0058	section 2.1 this study
h_2 (LLR): elastic, $\alpha = 0.1 - 0.4$	0.0441 ± 0.0058	section 2.1 this study
h_2 (LOLA): elastic, $\alpha = 0.3$	0.0353 ± 0.0031	section 2.1 this study
h_2 (LOLA): elastic, $\alpha = 0.1 - 0.4$	0.0346 ± 0.0033	section 2.1 this study

Table 6: Observed apparent resistivity (ρ_a) and error ($d\rho_a$) calculated from Apollo lunar day-side transfer functions (Hobbs et al., 1983).

Period (s)	ρ_a (Ωm)	$d\rho_a$ (Ωm)
100000.00	58.6	2.1
50000.00	113.9	4.0
33333.33	164.5	5.7
25000.00	209.8	7.4
20000.00	250.8	9.2
16666.67	288.7	11.0
14285.71	324.6	12.7
12500.00	358.9	13.9
11111.11	392.3	14.4
10000.00	424.8	14.2
5000.00	693.5	36.6
3333.33	921.4	70.5
2500.00	1099.2	91.9
2000.00	1212.7	109.6
1666.67	1283.2	110.8
1428.57	1350.8	96.8
1250.00	1471.7	82.3
1111.11	1542.5	74.5
1000.00	1674.9	84.3

Table 7: Data sets and prior information of internal structure model inversions. ISSI team seismological data sets and quake locations are summarized in our companion paper (Nunn et al., Submitted).

Model name	M1	M2	M3
Data / prior			
Body wave travel times	ISSI team data set	ISSI team data set	ISSI team data set (prediction)
Electromag. sounding	None	None	Table 6
Geodetic data	None	Table 5	Khan et al. (2014)
prior source locations	ISSI team compilation	ISSI team compilation	ISSI team compilation

Table 8: Summary of M1 model parameters and model parameter ranges (prior information).

Description	Quantity	Parameter	Value/Range	Distribution
Vp between surface and core	15		0.5 – 9.5 km/s	uniform
Vp/Vs ratio between surface and core	4		1.5 – 2.2	uniform
Core/mantle boundary depth	1		1200 – 1400 km	uniform
Core Vp	1		0.5 – 9.5 km/s	uniform
Core Vs	1		0 km/s	fixed
P-wave station corrections	4	T_{corP}	-4 – 4 s	inverted from travel times
S-wave station corrections	4	T_{corS}	-4 – 4 s	inverted from travel times

Table 9: Summary of M2 model parameters and model parameter ranges (prior information).

Description	Quantity	Parameter	Value/Range	Distribution
Crust density	1		2600 kg/m ³	fixed
Crust seismic model	NA	LG03	fixed	
Crustal thickness	1		30 – 45 km	uniform
Density Jump at crust-mantle boundary	1		400 – 00 kg/m ³	uniform
Base of lithosphere radius	1		600 – 1630 km	uniform
Excess thermal gradient in lithosphere	1		0 – 10 K/km	uniform
birch law parameter "a" (mantle)	1	a	-13 – -5 km/s	uniform
birch law parameter "b" (mantle)	1	b	3 – 7	uniform
Vp/Vs ratio at top of mantle	1		1.65 – 1.85	uniform
Vp/Vs ratio at 700 km radius	1		1.65 – 1.85	uniform
Vp/Vs ratio at bottom of mantle	1		1.65 – 1.85	uniform
Core radius	1		250 – 550 km	uniform
Core Vp	1		4.0 km/s	fixed
Core density	1		3000 - 8000 kg/m ³	deduced from Mass budget
P-wave station corrections	4	T_{corP}	-10–10 s	inverted from travel times
S-wave station corrections	4	T_{corS}	-10–10 s	inverted from travel times

Table 10: Summary of M3 model parameters and model parameter ranges (prior information).

Description	Quantity	Parameter	Value/Range	Distribution
Surface porosity	5	ϕ	0.4–0.75	uniform
Surface temperature	1	T_{surf}	0 °C	fixed
Crustal thickness	1	d_1	40 km	fixed
Upper mantle thickness	1	d_2	$d_1 < d_2 < d_3$	uniform
Lower mantle thickness	1	d_3	$d_2 < d_3 < 1737.151 \text{ km} - r_{core}$	uniform
Crustal composition (in the NCFMAS system)	5	X_1	Taylor et al. (2006) values given in Table caption	fixed
Upper mantle composition (in the NCFMAS system)	5	X_2	variable	uniform
Lower mantle composition (in the NCFMAS system)	5	X_3	variable	uniform
Temperature	40	T_i	variable	$T_{i-1} < T_i < T_{i+1}$
Core radius	1	r_{core}	0–434 km	uniform
Core density	1	ρ_{core}	$\rho_m = 7.5 \text{ g/cm}^3$	uniform
Core S-wave speed	1	V_S^{core}	0 km/s	fixed
Core P-wave speed	1	V_P^{core}	2–5 km/s	variable
Core electrical conductivity	1	σ_{core}	10^5 S/m	fixed

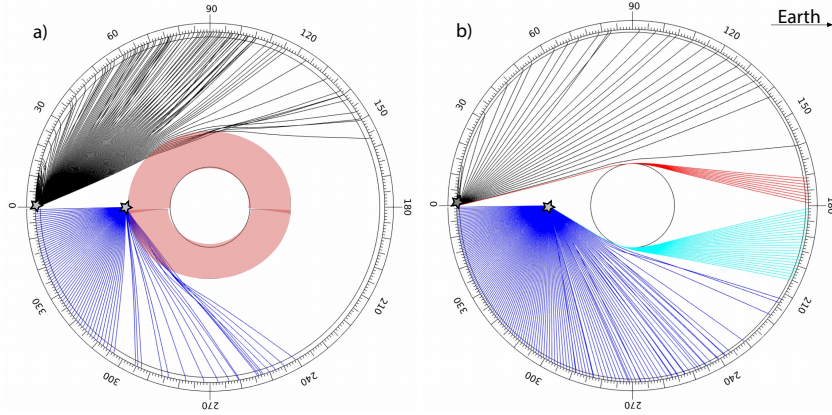


Fig. 12: Theoretical S-wave ray paths in models with and without a lower mantle low-velocity layer for a surface impact (gray star) and a deep moonquake (blue star), respectively. a) model M1 with a low-velocity lower mantle (red region surrounding the core) and b) model M2 without. For model M1, S-wave ray paths (black lines) are shown for a surface source and a source at 900 km (blue lines). For model M2, ray paths for S-waves are shown in black (surface source) and blue (source at 900 km depth) and for diffracted S-waves in red (surface source) and cyan (source at 900 km depth). The circle in the center marks the core in both plots. Plots were produced using the numerical software TTBox (Knapmeyer, 2004).

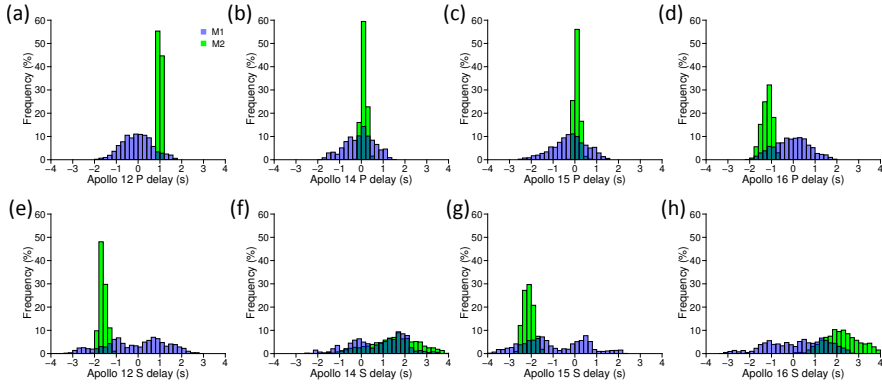


Fig. 13: Distributions of P -wave (a–d) and S -wave (e–h) station corrections for model suites M1 and M2. No station corrections were used for M3.

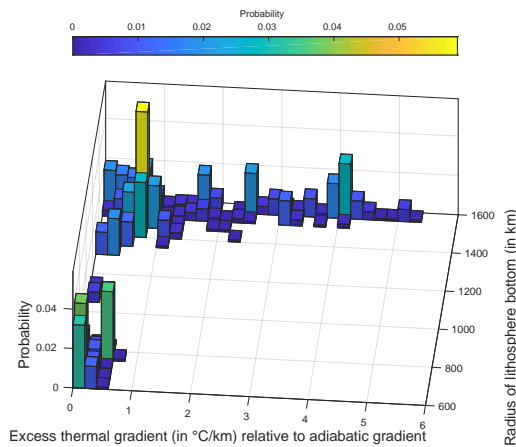


Fig. 14: 2D histogram of excess thermal gradient (in $^{\circ}\text{C}/\text{km}$) as a function of bottom radius of the lithosphere (in km) for the 1% best models of M2 inversion.

1071 8 Appendices**1072 .1 Appendix**

1073 This appendix provides the numerical values of the median of internal structure model distri-
1074 butions of M1, M2, and M3 inversions.

M1			M2				M3			
Depth (km)	V_P (km/s)	V_S (km/s)	Depth (km)	V_P (km/s)	V_S (km/s)	ρ (g/cm $^{-3}$)	Depth (km)	V_P (km/s)	V_S (km/s)	ρ (g/cm $^{-3}$)
0.00	4.04	2.32	0.00	1.00	0.50	2.60	0.00	4.50	2.47	2.60
10.00	4.65	2.68	1.00	1.00	0.50	2.60	20.00	5.70	3.12	2.76
20.00	5.26	3.05	1.00	3.20	1.80	2.60	40.00	6.73	3.71	2.89
30.00	5.90	3.42	12.00	3.20	1.80	2.60	60.00	7.62	4.30	3.23
40.00	6.51	3.79	12.00	5.50	3.30	2.60	80.00	7.62	4.30	3.23
50.00	7.10	4.12	28.00	5.50	3.30	2.60	100.00	7.63	4.31	3.23
60.00	7.57	4.38	28.00	7.68	4.41	3.34	120.00	7.80	4.45	3.35
70.00	7.62	4.42	41.63	7.68	4.41	3.34	140.00	7.80	4.45	3.35
80.00	7.63	4.42	65.40	7.68	4.40	3.34	160.00	7.80	4.45	3.36
90.00	7.64	4.42	90.00	7.67	4.39	3.34	180.00	7.80	4.44	3.36
100.00	7.64	4.42	110.00	7.66	4.39	3.34	200.00	7.81	4.44	3.36
110.00	7.64	4.41	132.01	7.66	4.39	3.34	220.00	7.81	4.44	3.36
120.00	7.64	4.41	140.59	7.67	4.39	3.34	240.00	7.88	4.48	3.36
130.00	7.64	4.41	176.44	7.68	4.39	3.34	260.00	7.98	4.52	3.41
140.00	7.64	4.40	180.99	7.69	4.40	3.35	280.00	8.03	4.53	3.42
150.00	7.63	4.40	201.10	7.70	4.41	3.35	300.00	8.03	4.53	3.42
160.00	7.63	4.39	224.75	7.71	4.41	3.35	320.00	8.04	4.53	3.42
170.00	7.63	4.39	243.07	7.72	4.42	3.35	340.00	8.04	4.53	3.42
180.00	7.63	4.38	275.40	7.74	4.43	3.36	360.00	8.04	4.53	3.42
190.00	7.62	4.38	290.00	7.75	4.43	3.36	380.00	8.05	4.53	3.42
200.00	7.62	4.38	310.00	7.76	4.44	3.36	400.00	8.05	4.53	3.42
210.00	7.62	4.38	330.00	7.78	4.45	3.36	420.00	8.05	4.53	3.43
220.00	7.62	4.38	350.00	7.79	4.45	3.37	440.00	8.05	4.53	3.43
230.00	7.62	4.37	370.00	7.80	4.46	3.37	460.00	8.05	4.53	3.43
240.00	7.62	4.37	390.00	7.82	4.47	3.37	480.00	8.05	4.53	3.43
250.00	7.62	4.37	410.00	7.83	4.47	3.37	500.00	8.06	4.53	3.43
260.00	7.62	4.37	429.66	7.84	4.48	3.38	520.00	8.06	4.53	3.43
270.00	7.62	4.37	446.83	7.85	4.49	3.38	540.00	8.06	4.53	3.43
280.00	7.63	4.37	488.22	7.86	4.50	3.38	560.00	8.06	4.53	3.43
290.00	7.64	4.37	495.88	7.87	4.50	3.38	580.00	8.06	4.53	3.43
300.00	7.64	4.37	501.10	7.88	4.51	3.39	600.00	8.06	4.53	3.43
310.00	7.65	4.37	514.69	7.89	4.51	3.39	620.00	8.06	4.53	3.43
320.00	7.65	4.37	542.72	7.91	4.52	3.39	640.00	8.06	4.53	3.44
330.00	7.66	4.38	563.71	7.92	4.53	3.39	660.00	8.06	4.53	3.44

340.00	7.67	4.38	585.59	7.93	4.53	3.39	680.00	8.06	4.52	3.44
350.00	7.68	4.38	619.69	7.94	4.54	3.40	700.00	8.06	4.52	3.44
360.00	7.69	4.39	639.98	7.95	4.54	3.40	720.00	8.06	4.52	3.44
370.00	7.70	4.39	650.00	7.96	4.55	3.40	740.00	8.06	4.52	3.44
380.00	7.71	4.39	670.00	7.97	4.55	3.40	760.00	8.05	4.51	3.44
390.00	7.72	4.40	690.00	7.98	4.56	3.40	780.00	8.06	4.51	3.44
400.00	7.73	4.40	710.00	7.99	4.56	3.41	800.00	8.05	4.51	3.44
410.00	7.74	4.41	735.10	8.00	4.57	3.41	820.00	8.05	4.51	3.44
420.00	7.75	4.41	750.00	8.01	4.57	3.41	840.00	8.05	4.51	3.44
430.00	7.76	4.42	775.40	8.02	4.57	3.41	860.00	8.05	4.51	3.44
440.00	7.77	4.42	790.00	8.02	4.58	3.41	880.00	8.04	4.50	3.44
450.00	7.78	4.43	810.00	8.03	4.58	3.41	900.00	8.04	4.50	3.44
460.00	7.79	4.43	830.00	8.04	4.59	3.42	920.00	8.04	4.49	3.44
470.00	7.80	4.44	850.00	8.05	4.59	3.42	940.00	8.04	4.49	3.44
480.00	7.81	4.44	870.00	8.06	4.59	3.42	960.00	8.03	4.49	3.44
490.00	7.82	4.45	890.00	8.06	4.60	3.42	980.00	8.03	4.48	3.44
500.00	7.84	4.45	910.00	8.07	4.60	3.42	1000.00	8.03	4.48	3.44
510.00	7.85	4.46	930.00	8.08	4.61	3.42	1020.00	8.02	4.48	3.44
520.00	7.86	4.46	950.00	8.09	4.61	3.43	1040.00	8.02	4.48	3.44
530.00	7.87	4.47	970.00	8.09	4.61	3.43	1060.00	8.02	4.48	3.44
540.00	7.88	4.47	990.00	8.10	4.61	3.43	1080.00	8.02	4.48	3.44
550.00	7.89	4.48	1010.00	8.11	4.62	3.43	1100.00	8.02	4.47	3.44
560.00	7.90	4.48	1030.00	8.11	4.62	3.43	1120.00	8.01	4.47	3.44
570.00	7.91	4.49	1050.00	8.12	4.63	3.43	1140.00	8.01	4.47	3.44
580.00	7.92	4.49	1070.00	8.12	4.63	3.43	1160.00	7.98	4.46	3.44
590.00	7.93	4.50	1090.00	8.13	4.64	3.44	1180.00	7.89	4.45	3.39
600.00	7.94	4.51	1110.00	8.14	4.65	3.44	1200.00	7.80	4.43	3.37
610.00	7.96	4.51	1130.00	8.14	4.66	3.44	1220.00	7.74	4.39	3.35
620.00	7.97	4.52	1150.00	8.15	4.66	3.44	1240.00	7.72	4.36	3.34
630.00	7.98	4.52	1170.00	8.15	4.67	3.44	1260.00	6.28	2.81	3.32
640.00	7.99	4.53	1190.00	8.16	4.68	3.44	1280.00	5.80	2.45	3.29
650.00	8.00	4.54	1210.00	8.16	4.69	3.44	1300.00	5.48	2.20	3.26
660.00	8.01	4.54	1230.00	8.17	4.69	3.44	1447.52	5.48	2.20	3.26
670.00	8.02	4.55	1237.10	8.17	4.70	3.44	1447.52	2.64	0.00	4.48
680.00	8.03	4.55	1237.10	8.18	4.70	3.44	1737.00	2.64	0.00	4.48
690.00	8.04	4.56	1257.10	8.18	4.68	3.45				
700.00	8.05	4.57	1277.10	8.17	4.58	3.45				

710.00	8.06	4.57	1297.10	8.14	4.52	3.45
720.00	8.08	4.58	1317.10	4.00	0.00	4.16
730.00	8.09	4.59	1337.10	4.00	0.00	4.38
740.00	8.10	4.59	1357.10	4.00	0.00	4.46
750.00	8.11	4.60	1377.10	4.00	0.00	4.54
760.00	8.13	4.61	1397.10	4.00	0.00	4.54
770.00	8.14	4.62	1417.10	4.00	0.00	4.55
780.00	8.15	4.62	1437.10	4.00	0.00	4.55
790.00	8.16	4.63	1457.10	4.00	0.00	4.55
800.00	8.17	4.64	1477.10	4.00	0.00	4.55
810.00	8.21	4.67	1497.10	4.00	0.00	4.55
820.00	8.22	4.67	1517.10	4.00	0.00	4.55
830.00	8.24	4.68	1537.10	4.00	0.00	4.55
840.00	8.24	4.69	1557.10	4.00	0.00	4.55
850.00	8.24	4.69	1577.10	4.00	0.00	4.55
860.00	8.24	4.69	1597.10	4.00	0.00	4.55
870.00	8.24	4.69	1617.10	4.00	0.00	4.55
880.00	8.24	4.69	1637.10	4.00	0.00	4.55
890.00	8.23	4.69	1657.10	4.00	0.00	4.55
900.00	8.23	4.68	1677.10	4.00	0.00	4.55
910.00	8.21	4.66	1697.10	4.00	0.00	4.55
920.00	8.17	4.63	1717.10	4.00	0.00	4.55
930.00	8.11	4.60	1737.10	4.00	0.00	4.55
940.00	8.05	4.57				
950.00	7.99	4.54				
960.00	7.92	4.51				
970.00	7.84	4.47				
980.00	7.76	4.44				
990.00	7.69	4.40				
1000.00	7.66	4.37				
1010.00	7.63	4.36				
1020.00	7.60	4.36				
1030.00	7.60	4.38				
1040.00	7.60	4.39				
1050.00	7.64	4.40				
1060.00	7.65	4.40				
1070.00	7.62	4.38				

1080.00	7.59	4.37
1090.00	7.57	4.37
1100.00	7.53	4.36
1110.00	7.52	4.35
1120.00	7.49	4.37
1130.00	7.49	4.39
1140.00	7.50	4.43
1150.00	7.51	4.45
1160.00	7.55	4.47
1170.00	7.56	4.49
1180.00	7.52	4.46
1190.00	7.54	4.45
1200.00	7.55	4.45
1210.00	7.36	4.36
1220.00	7.29	4.31
1230.00	7.24	4.24
1240.00	7.20	4.19
1250.00	7.12	4.12
1260.00	7.05	4.00
1270.00	6.99	3.93
1280.00	6.94	3.84
1290.00	6.88	3.73
1300.00	6.80	3.57
1310.00	6.71	0.00
1410.00	5.32	0.00
1510.00	5.32	0.00
1610.00	5.32	0.00
1710.00	5.32	0.00
1737.00	5.32	0.00

Table 11: Seismic velocity (in km/s) and density (in g/cm⁻³) models as a function of depth (in km) extracted from M1, M2 and M3 inversions. M1 and M2 models show the median values of the distributions, as well as the 1 σ uncertainties. For M3 the best misfit model is shown.

1075 **References**

- 1076 K. Aki, B. Chouet, Origin of coda waves: source, attenuation, and scattering effects. *Journal*
 1077 *of geophysical research* **80**(23), 3322–3342 (1975)
- 1078 D. Antonangeli, G. Morard, N.C. Schmerr, T. Komabayashi, M. Krisch, G. Fiquet, Y. Fei,
 1079 Toward a mineral physics reference model for the Moon's core. *Proceedings of the National*
 1080 *Academy of Sciences* (2015)
- 1081 J. Besserer, F. Nimmo, M.A. Wieczorek, R.C. Weber, W.S. Kiefer, P.J. McGovern, J.C.
 1082 Andrews-Hanna, D.E. Smith, M.T. Zuber, GRAIL gravity constraints on the vertical and
 1083 lateral density structure of the lunar crust. *Geophys. Res. Lett.* **41**, 5771–5777 (2014).
 1084 doi:10.1002/2014GL060240
- 1085 J.-F. Blanchette-Guertin, C.L. Johnson, J.F. Lawrence, Investigation of scattering in
 1086 lunar seismic coda. *Journal of Geophysical Research (Planets)* **117**, 06003 (2012).
 1087 doi:10.1029/2011JE004042
- 1088 J.-F. Blanchette-Guertin, C. Johnson, J. Lawrence, Modeling seismic energy propagation in
 1089 highly scattering environments. *Journal of Geophysical Research: Planets* **120**(3), 515–537
 1090 (2015)
- 1091 A.S. Buono, D. Walker, The Fe-rich liquidus in the Fe-FeS system from 1 bar to 10 GPa.
 1092 *Geochimica et Cosmochimica Acta* **75**(8), 2072–2087 (2011)
- 1093 H. Chi, R. Dasgupta, M.S. Duncan, N. Shimizu, Partitioning of carbon between Fe-rich alloy
 1094 melt and silicate melt in a magma ocean –Implications for the abundance and origin of
 1095 volatiles in Earth, Mars, and the Moon. *Geochimica et Cosmochimica Acta* **139**(Supplement
 1096 C), 447–471 (2014)
- 1097 J.A.D. Connolly, The geodynamic equation of state: What and how. *Geochemistry, Geophysics,*
 1098 *Geosystems* **10**(10), (2009). Q10014. doi:10.1029/2009GC002540
- 1099 M.R. Cooper, R.L. Kovach, J.S. Watkins, Lunar near-surface structure. *Reviews of Geophysics*
 1100 and Space Physics
- 1101 A.M. Dainty, N.R. Goins, M.N. Toksöz, Seismic investigation of the lunar interior, vol. 7 1976a,
 1102 p. 181
- 1103 A.M. Dainty, M.N. Toköz, S. Stein, Seismic investigation of the lunar interior, vol. 3 1976b,
 1104 pp. 3057–3075
- 1105 A.M. Dainty, M.N. Toksöz, K.R. Anderson, P.J. Pines, Y. Nakamura, G. Latham, Seismic
 1106 Scattering and Shallow Structure of the Moon in Oceanus Procellarum. *Moon* **9**, 11–29
 1107 (1974). doi:10.1007/BF00565388
- 1108 M. Drilleau, . Beucler, A. Mocquet, O. Verhoeven, G. Moebs, G. Burgos, J.-P. Montagner,
 1109 P. Vacher, A bayesian approach to infer radial models of temperature and anisotropy in
 1110 the transition zone from surface wave dispersion curves. *Geophysical Journal International*
 1111 **195**(2), 1165–1183 (2013). doi:10.1093/gji/ggt284
- 1112 A. Duba, H.C. Heard, R.N. Schock, Electrical conductivity of orthopyroxene to 1400 C and the
 1113 resulting selenotherm, in *Lunar and Planetary Science Conference Proceedings*, ed. by D.C.
 1114 Kinsler *Lunar and Planetary Science Conference Proceedings*, vol. 7, 1976, pp. 3173–3181
- 1115 F. Duennenbier, G.H. Sutton, Thermal moonquakes. *J. Geophys. Res.* **79**, 4351–4363 (1974).
 1116 doi:10.1029/JB079i029p04351
- 1117 P. Dyal, C.W. Parkin, W.D. Daily, Structure of the lunar interior from magnetic field mea-
 1118 surements, in *Lunar and Planetary Science Conference Proceedings*, ed. by D.C. Kinsler
 1119 *Lunar and Planetary Science Conference Proceedings*, vol. 7, 1976, pp. 3077–3095
- 1120 M. Efroimsky, Bodily tides near spin-orbit resonances. *Celestial Mechanics and Dynamical*
 1121 *Astronomy* **112**, 283–330 (2012a). doi:10.1007/s10569-011-9397-4
- 1122 M. Efroimsky, Tidal Dissipation Compared to Seismic Dissipation: In Small Bodies,
 1123 Earths, and Super-Earths. *The Astrophysical Journal* **746**, 150 (2012b). doi:10.1088/0004-
 1124 637X/746/2/150
- 1125 Y. Fei, E. Brosh, Experimental study and thermodynamic calculations of phase relations in
 1126 the Fe–C system at high pressure. *Earth and Planetary Science Letters* **408**(0), 155–162
 1127 (2014)
- 1128 C. Frohlich, Y. Nakamura, Possible extra-Solar-System cause for certain lunar seismic events.
 1129 *Icarus* **185**, 21–28 (2006). doi:10.1016/j.icarus.2006.07.002
- 1130 J. Gagnepain-Beyneix, P. Lognonné, H. Chenet, D. Lombardi, T. Spohn, A seismic model of
 1131 the lunar mantle and constraints on temperature and mineralogy. *Physics of the Earth and*
 1132 *Planetary Interiors* **159**, 140–166 (2006). doi:10.1016/j.pepi.2006.05.009
- 1133 R. Garcia, H. Tkalčić, S. Chevrot, A new global PKP data set to study Earth's core and deep

- mantle. *Phys. Earth Planet. Inter.* **159**, 15–31 (2006)
- R.F. Garcia, J. Gagnepain-Beyneix, S. Chevrot, P. Lognonné, Very preliminary reference Moon model. *Physics of the Earth and Planetary Interiors* **188**, 96–113 (2011). doi:10.1016/j.pepi.2011.06.015
- M.S. Ghiorso, M.M. Hirschmann, P.W. Reiners, V.C. Kress III, The pmelets: A revision of melts for improved calculation of phase relations and major element partitioning related to partial melting of the mantle to 3 gpa. *Geochemistry, Geophysics, Geosystems* **3**(5), 1–35 (2002). doi:10.1029/2001GC000217. <https://agupubs.onlinelibrary.wiley.com/doi/abs/10.1029/2001GC000217>
- K. Gillet, L. Margerin, M. Calvet, M. Monnereau, Scattering attenuation profile of the Moon: Implications for shallow moonquakes and the structure of the megaregolith. *Physics of the Earth and Planetary Interiors* **262**, 28–40 (2017). doi:10.1016/j.pepi.2016.11.001
- N.R. Goins, Lunar seismology: The internal structure of the moon. Ph.D. thesis, Mass. Inst. of Technol., Cambridge (1978)
- N.R. Goins, A.M. Dainty, M.N. Toksoz, Lunar seismology - The internal structure of the moon. *J. Geophys. Res.* **86**, 5061–5074 (1981). doi:10.1029/JB086iB06p50561
- D.H. Green, N.G. Ware, W.O. Hibberson, A. Major, Experimental petrology of Apollo 12 basalts: part 1, sample 12009. *Earth and Planetary Science Letters* **13**(1), 85–96 (1971)
- Y. Harada, S. Goossens, K. Matsumoto, J. Yan, J. Ping, H. Noda, J. Haruyama, Strong tidal heating in an ultralow-viscosity zone at the core-mantle boundary of the Moon. *Nature Geoscience* **7**, 569–572 (2014). doi:10.1038/ngeo2211
- E.H. Hauri, A.E. Saal, M.J. Rutherford, J.A. Van Orman, Water in the Moon's interior: Truth and consequences. *Earth and Planetary Science Letters* **409**, 252–264 (2015). doi:10.1016/j.epsl.2014.10.053
- S. Hempel, M. Knapmeyer, A.R.T. Jonkers, J. Oberst, Uncertainty of Apollo deep moonquake locations and implications for future network designs. *Icarus* **220**, 971–980 (2012)
- B.A. Hobbs, L.L. Hood, F. Herbert, C.P. Sonett, An upper bound on the radius of a highly electrically conducting lunar core. *J. Geophys. Res.* **88**, 97–102 (1983). doi:10.1029/JB088iS01p00B97
- L.L. Hood, Geophysical constraints on the lunar interior, in *Origin of the Moon*, ed. by W.K. Hartmann, R.J. Phillips, G.J. Taylor, 1986, pp. 361–410
- L.L. Hood, M.T. Zuber, Recent Refinements in Geophysical Constraints on Lunar Origin and Evolution, ed. by R.M. Canup, K. Righter, et al. 2000, pp. 397–409
- L.L. Hood, F. Herbert, C.P. Sonett, The deep lunar electrical conductivity profile - Structural and thermal inferences. *J. Geophys. Res.* **87**, 5311–5326 (1982). doi:10.1029/JB087iB07p05311
- L.L. Hood, D.L. Mitchell, R.P. Lin, M.H. Acuna, A.B. Binder, Initial measurements of the lunar induced magnetic dipole moment using Lunar Prospector magnetometer data. *Geophys. Res. Lett.* **26**, 2327–2330 (1999). doi:10.1029/1999GL900487
- P. Horvath, Analysis of lunar seismic signals—Determination of instrumental parameters and seismic velocity distribution. Ph.D. thesis, Univ. of Tex. at Dallas, Richardson (1979)
- J.S. Huebner, A. Duba, L.B. Wiggins, Electrical conductivity of pyroxene which contains trivalent cations - Laboratory measurements and the lunar temperature profile. *J. Geophys. Res.* **84**, 4652–4656 (1979). doi:10.1029/JB084iB09p04652
- Z. Jing, Y. Wang, Y. Kono, T. Yu, T. Sakamaki, C. Park, M.L. Rivers, S.R. Sutton, G. Shen, Sound velocity of Fe–S liquids at high pressure: Implications for the Moon's molten outer core. *Earth and Planetary Science Letters* **396**(0), 78–87 (2014)
- H. Kanamori, A. Nur, D. Chung, D. Wones, G. Simmons, Elastic wave velocities of lunar samples at high pressures and their geophysical implications. *Science* **167**, 726–728 (1970)
- S.-i. Karato, Water distribution across the mantle transition zone and its implications for global material circulation. *Earth and Planetary Science Letters* **301**, 413–423 (2011). doi:10.1016/j.epsl.2010.11.038
- S.-i. Karato, Geophysical constraints on the water content of the lunar mantle and its implications for the origin of the Moon. *Earth and Planetary Science Letters* **384** (2013). doi:10.1016/j.epsl.2013.10.001
- T. Kawamura, N. Kobayashi, S. Tanaka, P. Lognonné, Lunar Surface Gravimeter as a lunar seismometer: Investigation of a new source of seismic information on the Moon. *Journal of Geophysical Research (Planets)* **120**, 343–358 (2015). doi:10.1002/2014JE004724
- A. Khan, K. Mosegaard, An inquiry into the lunar interior: A nonlinear inversion of the Apollo lunar seismic data. *Journal of Geophysical Research (Planets)* **107**, 3–1 (2002).

- 1194 doi:10.1029/2001JE001658
1195 A. Khan, K. Mosegaard, Further constraints on the deep lunar interior. *Geophys. Res. Lett.*
1196 **32**, 22203 (2005). doi:10.1029/2005GL023985
1197 A. Khan, T.J. Shankland, A geophysical perspective on mantle water content and melting:
1198 Inverting electromagnetic sounding data using laboratory-based electrical conductivity pro-
1199 files. *Earth and Planetary Science Letters* **317**, 27–43 (2012). doi:10.1016/j.epsl.2011.11.031
1200 A. Khan, K. Mosegaard, K.L. Rasmussen, A new seismic velocity model for the Moon from a
1201 Monte Carlo inversion of the Apollo lunar seismic data. *Geophys. Res. Lett.* **27**, 1591–1594
1202 (2000). doi:10.1029/1999GL008452
1203 A. Khan, K. Mosegaard, J.G. Williams, P. Lognonné, Does the Moon possess a molten core?
1204 Probing the deep lunar interior using results from LLR and Lunar Prospector. *Journal of*
1205 *Geophysical Research (Planets)* **109**, 09007 (2004). doi:10.1029/2004JE002294
1206 A. Khan, J. MacLennan, S.R. Taylor, J.A.D. Connolly, Are the earth and the moon com-
1207 positionally alike? inferences on lunar composition and implications for lunar origin and
1208 evolution from geophysical modeling. *Journal of Geophysical Research: Planets* **111**(E5),
1209 (2006a). E05005. doi:10.1029/2005JE002608. <http://dx.doi.org/10.1029/2005JE002608>
1210 A. Khan, J.A.D. Connolly, N. Olsen, K. Mosegaard, Constraining the com-
1211 position and thermal state of the moon from an inversion of electromag-
1212 netic lunar day-side transfer functions. *Earth and Planetary Science Let-
1213 ters* **248**(3), 579–598 (2006b). doi:<https://doi.org/10.1016/j.epsl.2006.04.008>.
1214 <http://www.sciencedirect.com/science/article/pii/S0012821X06002937>
1215 A. Khan, J.A.D. Connolly, J. MacLennan, K. Mosegaard, Joint inversion of seismic and gravity
1216 data for lunar composition and thermal state. *Geophysical Journal International* **168**, 243–
1217 258 (2007). doi:10.1111/j.1365-246X.2006.03200.x
1218 A. Khan, A. Pommier, G.A. Neumann, K. Mosegaard, The lunar moho and the internal
1219 structure of the moon: A geophysical perspective. *Tectonophysics* **609**, 331–352 (2013).
1220 Moho: 100 years after Andrija Mohorovicic. doi:<https://doi.org/10.1016/j.tecto.2013.02.024>.
1221 <http://www.sciencedirect.com/science/article/pii/S0040195113001236>
1222 A. Khan, J.A.D. Connolly, A. Pommier, J. Noir, Geophysical evidence for melt
1223 in the deep lunar interior and implications for lunar evolution. *Journal of Geo-
1224 physical Research: Planets* **119**(10), 2197–2221 (2014). doi:10.1002/2014JE004661.
1225 <http://dx.doi.org/10.1002/2014JE004661>
1226 M. Knapmeyer, TTBox: A MatLab Toolbox for the Computation of 1D Teleseismic Travel
1227 Times. *Seismological Research Letters* **75**(6), 726–733 (2004). doi:10.1785/gssrl.75.6.726.
1228 <https://dx.doi.org/10.1785/gssrl.75.6.726>
1229 T. Komabayashi, Thermodynamics of melting relations in the system Fe-FeO at high pressure:
1230 Implications for oxygen in the Earth's core. *Journal of Geophysical Research: Solid Earth*,
1231 2014–010980 (2014)
1232 A.S. Konopliv, R.S. Park, D.-N. Yuan, S.W. Asmar, M.M. Watkins, J.G. Williams, E. Fahne-
1233 stock, G. Kruizinga, M. Paik, D. Strekalov, N. Harvey, D.E. Smith, M.T. Zuber, The JPL
1234 lunar gravity field to spherical harmonic degree 660 from the GRAIL primary mission. *J.*
1235 *Geophys. Res. Planets*, 1415–1434 (2013). doi:10.1002/jgre.20097
1236 R.L. Kovach, J.S. Watkins, Apollo 17 Seismic Profiling: Probing the Lunar Crust. *Science* **180**,
1237 1063–1064 (1973a). doi:10.1126/science.180.4090.1063
1238 R.L. Kovach, J.S. Watkins, The structure of the lunar crust at the Apollo 17 site, in *Lunar*
1239 *and Planetary Science Conference Proceedings*. Lunar and Planetary Science Conference
1240 Proceedings, vol. 4, 1973b, p. 2549
1241 V.A. Kronrod, O.L. Kuskov, Inversion of seismic and gravity data for the composition
1242 and core sizes of the Moon. *Izvestiya Physics of the Solid Earth* **47**, 711–730 (2011).
1243 doi:10.1134/S1069351311070044
1244 O.L. Kuskov, D.K. Belashchenko, Thermodynamic properties of Fe-S alloys from molecular
1245 dynamics modeling: Implications for the lunar fluid core. *Physics of the Earth and Planetary*
1246 *Interiors* **258**, 43–50 (2016). doi:10.1016/j.pepi.2016.07.006
1247 O.L. Kuskov, V.A. Kronrod, Constitution of the Moon5. Constraints on composition, density,
1248 temperature, and radius of a core. *Physics of the Earth and Planetary Interiors* **107**, 285–306
1249 (1998). doi:10.1016/S0031-9201(98)00082-X
1250 O.L. Kuskov, V.A. Kronrod, Geochemical constraints on the model of the composition and
1251 thermal conditions of the Moon according to seismic data. *Izvestiya Physics of the Solid*
1252 *Earth* **45**, 753–768 (2009). doi:10.1134/S1069351309090043
1253 D.R. Lammlein, Lunar seismicity and tectonics. *Physics of the Earth and Planetary Interiors*

- 1254 **14**, 224–273 (1977). doi:10.1016/0031-9201(77)90175-3
1255 M. Laneuville, J. Taylor, M.A. Wieczorek, Distribution of radioactive heat sources and thermal
1256 history of the Moon. *J. Geophys. Res. Planets* **in press** (2019). doi:10.1029/2018JE005742
1257 M. Laneuville, M.A. Wieczorek, D. Breuer, N. Tosi, Asymmetric thermal evolution
1258 of the Moon. *Journal of Geophysical Research (Planets)* **118**, 1435–1452 (2013).
1259 doi:10.1002/jgre.20103
1260 M. Laneuville, M.A. Wieczorek, D. Breuer, J. Aubert, G. Morard, T. Rückriemen, A long-lived
1261 lunar dynamo powered by core crystallization. *Earth and Planetary Science Letters* **401**(0),
1262 251–260 (2014)
1263 E. Larose, A. Khan, Y. Nakamura, M. Campillo, Lunar subsurface investigated from correlation
1264 of seismic noise. *Geophys. Res. Lett.* **32**, 16201 (2005). doi:10.1029/2005GL023518
1265 G.V. Latham, M. Ewing, F. Press, G. Sutton, J. Dorman, Y. Nakamura, N. Toksöz, R. Wiggins,
1266 J. Derr, F. Duennebier, Passive seismic experiment. *Science* **167**(3918), 455–457 (1970a).
1267 DOI: 10.1126/science.167.3918.455
1268 G. Latham, M. Ewing, J. Dorman, F. Press, N. Toksöz, G. Sutton, R. Meissner, F. Duennebier,
1269 Y. Nakamura, R. Kovach, M. Yates, Seismic data from man-made impacts on the moon.
1270 *Science* **170**(3958), 620–626 (1970b). DOI: 10.1126/science.170.3958.620
1271 F.G. Lemoine, S. Goossens, T.J. Sabaka, J.B. Nicholas, E. Mazarico, D.D. Rowlands, B.D.
1272 Loomis, D.S. Chinn, D.S. Caprette, G.A. Neumann, D.E. Smith, M.T. Zuber, High-degree
1273 gravity models from GRAIL primary mission data. *J. Geophys. Res. Planets* **118**, 1676–1698
1274 (2013). doi:10.1002/jgre.20118
1275 F.G. Lemoine, S. Goossens, T.J. Sabaka, J.B. Nicholas, E. Mazarico, D.D. Rowlands, B.D.
1276 Loomis, D.S. Chinn, G.A. Neumann, D.E. Smith, M.T. Zuber, GRGM900C: A degree 900
1277 lunar gravity model from GRAIL primary and extended mission data. *Geophys. Res. Lett.*
1278 **41**, 3382–3389 (2014). doi:10.1002/2014GL060027
1279 P. Lognonné, C.L. Johnson, Planetary Seismology. *Treatise on Geophysics* **10**, 69–122 (2007)
1280 P. Lognonné, J. Gagnepain-Beyneix, H. Chenet, A new seismic model of the Moon: implications
1281 for structure, thermal evolution and formation of the Moon. *Earth and Planetary Science
Letters* **211**, 27–44 (2003). doi:10.1016/S0012-821X(03)00172-9
1282 J. Longhi, Petrogenesis of picritic mare magmas: Constraints on the extent of early lunar
1283 differentiation. *Geochimica et Cosmochimica Acta* **70**(24), 5919–5934 (2006)
1284 L. Margerin, G. Nolet, Multiple scattering of high-frequency seismic waves in the deep earth:
1285 Modeling and numerical examples. *Journal of Geophysical Research: Solid Earth* **108**(B5)
1286 (2003)
1287 K. Matsumoto, R. Yamada, F. Kikuchi, S. Kamata, Y. Ishihara, T. Iwata, H. Hanada, S. Sasaki,
1288 Internal structure of the Moon inferred from Apollo seismic data and selenodetic data from
1289 GRAIL and LLR. *Geophys. Res. Lett.* **42**, 7351–7358 (2015). doi:10.1002/2015GL065335
1290 I. Matsuyama, F. Nimmo, J.T. Keane, N.H. Chan, G.J. Taylor, M.A. Wieczorek, W.S. Kiefer,
1291 J.G. Williams, Grail, llr, and lola constraints on the interior structure of the moon. *Geophys.
Res. Lett.* **43**, 8365–8375 (2016). doi:10.1002/2016GL069952
1292 E. Mazarico, M.K. Barker, G.A. Neumann, M.T. Zuber, , D.E. Smith, Detection of the lunar
1293 body tide by the Lunar Orbiter Laser Altimeter. *Geophys. Res. Lett.* **41**, 2282–2288 (2014).
1294 doi:10.1002/2013GL059085
1295 K. Miljković, M.A. Wieczorek, G.S. Collins, S.C. Solomon, D.E. Smith, M.T. Zuber, Excavation
1296 of the lunar mantle by basin-forming impact events on the Moon. *Earth Planet. Sci. Lett.*
1297 **409**, 243–251 (2015). doi:10.1016/j.epsl.2014.10.041
1298 G. Morard, J. Bouchet, A. Rivoldini, D. Antonangeli, M. Roberge, E. Boulard, A. Denoeud,
1299 M. Mezouar, Liquid properties in the Fe-FeS system under moderate pressure: tool box to
1300 model small planetary cores. *American Mineralogist* (2018)
1301 K. Mosegaard, A. Tarantola, Monte carlo sampling of solutions to inverse problems. *Journal of
1302 Geophysical Research: Solid Earth* **100**(B7), 12431–12447 (1995). doi:10.1029/94JB03097
1303 Y. Nakamura, Seismic energy transmission in the lunar surface zone determined from signals
1304 generated by movement of lunar rovers. *Bull. Seismol. Soc. Am.* **66**, 593–606 (1976)
1305 Y. Nakamura, Seismic velocity structure of the lunar mantle. *J. Geophys. Res.* **88**, 677–686
1306 (1983). doi:10.1029/JB088iB01p00677
1307 Y. Nakamura, Farside deep moonquakes and deep interior of the Moon. *Journal OF Geophys-
1308 ical Research* **110**, 01001–1010292004002332 (2005)
1309 Y. Nakamura, Planetary seismology: Early observational results, ed. by V.C.H.
1310 Tong, R.A.E. Garca (Cambridge University Press, 2015), pp. 91–106.
1311 doi:10.1017/CBO9781107300668.010

- 1314 Y. Nakamura, J. Koyama, Seismic Q of the lunar upper mantle. *J. Geophys. Res.* **87**, 4855–4861
1315 (1982). doi:10.1029/JB087iB06p04855
- 1316 Y. Nakamura, G.V. Latham, H.J. Dorman, Apollo lunar seismic experiment - Final sum-
1317 mary, in *Lunar and Planetary Science Conference Proceedings*, ed. by W. V. Boynton &
1318 T. J. Ahrens Lunar and Planetary Science Conference Proceedings, vol. 13, 1982, p. 117
- 1319 Y. Nakamura, D. Lammlein, G. Latham, M. Ewing, J. Dorman, F. Press, N. Toksoz,
1320 New Seismic Data on the State of the Deep Lunar Interior. *Science* **181**, 49–51 (1973).
1321 doi:10.1126/science.181.4094.49
- 1322 Y. Nakamura, G. Latham, D. Lammlein, M. Ewing, F. Duennbier, J. Dorman, Deep lu-
1323 nar interior inferred from recent seismic data. *Geophys. Res. Lett.* **1**, 137–140 (1974).
1324 doi:10.1029/GL001i003p00137
- 1325 Y. Nakamura, F.K. Duennbier, G.V. Latham, H.J. Dorman, Structure of the lunar mantle.
1326 *J. Geophys. Res.* **81**, 4818–4824 (1976). doi:10.1029/JB081i026p04818
- 1327 Y. Nakamura, G.V. Latham, H.J. Dorman, A.-B.K. Ibrahim, J. Koyama, P. Horvath, Shallow
1328 moonquakes - Depth, distribution and implications as to the present state of the lunar
1329 interior. *Lunar and Planetary Science Conference*, 10th, Houston, Tex., March 19-23, 1979,
1330 *Proceedings*, **3**, 2299–2309 (1979)
- 1331 F. Nimmo, U.H. Faul, E.J. Garnero, Dissipation at tidal and seismic frequencies in a melt-free
1332 moon. *J. Geophys. Res.* **117**, 09005 (2012). doi:10.1029/2012JE004160
- 1333 K. Nishida, A. Suzuki, H. Terasaki, Y. Shibasaki, Y. Higo, S. Kuwabara, Y. Shimoyama, M.
1334 Sakurai, M. Ushioda, E. Takahashi, T. Kikegawa, D. Wakabayashi, N. Funamori, Towards a
1335 consensus on the pressure and composition dependence of sound velocity in the liquid Fe–S
1336 system. *Physics of the Earth and Planetary Interiors* **257**, 230–239 (2016)
- 1337 C. Nunn, R.F. Garcia, , Y. Nakamura, A.G. Marusiak, T. Kawamura, D. Sun, L. Margerin, R.
1338 Weber, , M. Drilleau, M.A. Wieczorek, A. Khan, A. Rivoldini, P. Lognonne, P. Zhu, *Lunar
1339 seismology: a data and instrumentation review*. *Space Science Reviews*, (Submitted)
- 1340 J. Oberst, Meteoroids near the Earth-Moon System as Inferred from Temporal and Spatial
1341 Distribution of Impacts Detected by the Lunar Seismic Network. Ph.D. thesis, Univ. of Tex.
1342 at Austin (1989)
- 1343 J.-P. Poirier, *Introduction to the Physics of the Earth's Interior* 2000, p. 326
- 1344 N. Rai, W. van Westrenen, Lunar core formation: New constraints from metal–silicate parti-
1345 tioning of siderophile elements. *Earth and Planetary Science Letters* **388**(0), 343–352 (2014)
- 1346 A. Ricolleau, Y. Fei, A. Corgne, J. Siebert, J. Badro, Oxygen and silicon contents of Earth's
1347 core from high pressure metal-silicate partitioning experiments. *Earth and Planetary Science
1348 Letters* **310**(3-4), 409–421 (2011)
- 1349 K. Righter, M.J. Drake, Core Formation in Earth's Moon, Mars, and Vesta. *Icarus* **124**, 513–
1350 529 (1996)
- 1351 K. Righter, B.M. Go, K.A. Pando, L. Danielson, D.K. Ross, Z. Rahman, L.P. Keller, Phase
1352 equilibria of a low S and C lunar core: Implications for an early lunar dynamo and physical
1353 state of the current core. *Earth and Planetary Science Letters* **463**, 323–332 (2017)
- 1354 M. Sambridge, Geophysical inversion with a neighbourhood algorithm-I. Searching a param-
1355 eter space. *Geophysical Journal International* **138**, 479–494 (1999). doi:10.1046/j.1365-
1356 246X.1999.00876.x
- 1357 H. Sato, M.C. Fehler, T. Maeda, *Seismic Wave Propagation and Scattering in the Heteroge-
1358 neous Earth* (Springer Science & Business Media, ???, 2012)
- 1359 A. Scheinberg, K.M. Soderlund, G. Schubert, Magnetic field generation in the lunar core: The
1360 role of inner core growth. *Icarus* **254**, 62–71 (2015)
- 1361 P.C. Sellers, Seismic evidence for a low-velocity lunar core. *J. Geophys. Res.* **97**, 11663–11672
1362 (1992)
- 1363 C. Sens-Schönfelder, E. Larose, Temporal changes in the lunar soil from correlation of diffuse
1364 vibrations. *Phys. Rev. E* **78**(4), 045601 (2008). doi:10.1103/PhysRevE.78.045601
- 1365 P.M. Shearer, *Introduction to Seismology*, 2nd edn. (Cambridge University Press, ???, 2009).
1366 doi:10.1017/CBO9780511841552
- 1367 H. Shimizu, M. Matsushima, F. Takahashi, H. Shibuya, H. Tsunakawa, Constraint on the lunar
1368 core size from electromagnetic sounding based on magnetic field observations by an orbiting
1369 satellite. *Icarus* **222**, 32–43 (2013). doi:10.1016/j.icarus.2012.10.029
- 1370 Y. Shimoyama, H. Terasaki, S. Urakawa, Y. Takubo, S. Kuwabara, S. Kishimoto, T. Watanuki,
1371 A. Machida, Y. Katayama, T. Kondo, Thermoelastic properties of liquid Fe-C revealed by
1372 sound velocity and density measurements at high pressure. *Journal of Geophysical Research:
Solid Earth* **121**(11), 7984–7995 (2016)

- 1374 D.E. Smith, M.T. Zuber, G.B. Jackson, J.F. Cavanaugh, G.A. Neumann, H. Riris, X. Sun,
1375 R.S. Zellar, C. Coltharp, J. Connelly, R.B. Katz, I. Kleyner, P. Liiva, A. Matuszeski, E.M.
1376 Mazarico, J.F. McGarry, A.-M. Novo-Gradac, M.N. Ott, C. Peters, L.A. Ramos-Izquierdo,
1377 L. Ramsey, D.D. Rowlands, S. Schmidt, V.S. Scott, G.B. Shaw, J.C. Smith, J.-P. Swinski,
1378 M.H. Torrence, G. Unger, A.W. Yu, T.W. Zagwodzki, The Lunar Orbiter Laser Altimeter
1379 investigation on the Lunar Reconnaissance Orbiter mission. *Space Sci. Rev.* **150**, 209–241
1380 (2010). doi:10.1007/s11214-009-9512-y
- 1381 D. Sollberger, C. Schmelzbach, J.O.A. Robertsson, S.A. Greenhalgh, Y.
1382 Nakamura, A. Khan, The shallow elastic structure of the lunar crust:
1383 New insights from seismic wavefield gradient analysis. *Geophysical Re-*
1384 *search Letters* **43**(19), 10078–10087 (2016). doi:10.1002/2016GL070883.
1385 <https://agupubs.onlinelibrary.wiley.com/doi/abs/10.1002/2016GL070883>
- 1386 C.P. Sonett, Electromagnetic induction in the moon. *Reviews of Geophysics and Space Physics*
1387 **20**, 411–455 (1982). doi:10.1029/RG020i003p00411
- 1388 F.D. Stacey, P.M. Davis, *Physics of the Earth* 2008
- 1389 E.S. Steenstra, A.X. Seegers, J. Eising, B.G.J. Tomassen, F.P.F. Webers, J. Berndt, S. Klemme,
1390 S. Matveev, W. van Westrenen, Evidence for a sulfur-undersaturated lunar interior from the
1391 solubility of sulfur in lunar melts and sulfide-silicate partitioning of siderophile elements.
1392 *Geochimica et Cosmochimica Acta* **231**, 130–156 (2018)
- 1393 E.S. Steenstra, Y. Lin, N. Rai, M. Jansen, W. van Westrenen, Carbon as the dominant light
1394 element in the lunar core. *American Mineralogist* **102**(1), 92 (2017)
- 1395 L. Stixrude, C. Lithgow-Bertelloni, Thermodynamics of mantle minerals - I. Physical
1396 properties. *Geophysical Journal International* **162**, 610–632 (2005). doi:10.1111/j.1365-
1397 246X.2005.02642.x
- 1398 S.R. Taylor, G.J. Taylor, L.A. Taylor, The Moon: A Taylor perspective. *Geochimica et Cos-*
1399 *mochimica Acta* **70**, 5904–5918 (2006). doi:10.1016/j.gca.2006.06.262
- 1400 B. Tittmann, Lunar rock Q in 3000–5000 range achieved in laboratory. *Philosophical Transac-*
1401 *tions of the Royal Society of London A: Mathematical, Physical and Engineering Sciences*
1402 **285**(1327), 475–479 (1977)
- 1403 B. Tittmann, M. Abdel-Gawad, R. Housley, Elastic velocity and Q factor measurements on
1404 Apollo 12, 14, and 15 rocks, in *Lunar and Planetary Science Conference Proceedings*, vol.
1405 3, 1972, pp. 2565–2575
- 1406 B. Tittmann, L. Ahlberg, J. Curnow, Internal friction and velocity measurements, in *Lunar*
1407 *and Planetary Science Conference Proceedings*, vol. 7, 1976, pp. 3123–3132
- 1408 B. Tittmann, J. Curnow, R. Housley, Internal friction quality factor Q greater than or equal
1409 to 3100 achieved in lunar rock 70215, 85, in *Lunar and Planetary Science Conference*
1410 *Proceedings*, vol. 6, 1975, pp. 3217–3226
- 1411 B. Tittmann, H. Nadler, J. Richardson, L. Ahlberg, Laboratory measurements of p-wave seis-
1412 mic Q on lunar and analog rocks, in *Lunar and Planetary Science Conference Proceedings*,
1413 vol. 9, 1978, pp. 3627–3635
- 1414 M.N. Toksoz, A.M. Dainty, S.C. Solomon, K.R. Anderson, Structure of the moon. *Reviews of*
1415 *Geophysics and Space Physics* **12**, 539–567 (1974)
- 1416 H. Urey, *The Planets: Their Origin and Development* (Yale University Press, ???, 1952), p.
1417 245
- 1418 M. van Kan Parker, C. Sanloup, N. Sator, B. Guillot, E.J. Tronche, J.-P. Perrillat, M. Mezouar,
1419 N. Rai, W. van Westrenen, Neutral buoyancy of titanium-rich melts in the deep lunar
1420 interior. *Nature Geoscience* **5**, 186–189 (2012). doi:10.1038/ngeo1402
- 1421 L. Vinnik, H. Chenet, J. Gagnepain-Beyneix, P. Lognonné, First seismic receiver functions on
1422 the Moon. *Geophys. Res. Lett.* **28**, 3031–3034 (2001). doi:10.1029/2001GL012859
- 1423 H. Wang, T. Todd, D. Weidner, G. Simmons, Elastic properties of Apollo 12 rocks, in *Lunar*
1424 *and Planetary Science Conference Proceedings*, vol. 2, 1971, pp. 2327–2336
- 1425 N. Warren, E. Schreiber, C. Scholz, J. Morrison, P. Norton, M. Kumazawa, O. Anderson,
1426 Elastic and thermal properties of Apollo 11 and Apollo 12 rocks, in *Lunar and Planetary*
1427 *Science Conference Proceedings*, vol. 2, 1971, p. 2345
- 1428 R.C. Weber, P. Lin, E.J. Garnero, Q. Williams, P. Lognonné, Seismic Detection of the Lunar
1429 Core. *Science* **331**, 309 (2011). doi:10.1126/science.1199375
- 1430 M.A. Wieczorek, Gravity and topography of the terrestrial planets, in *Treatise on Geophysics*
1431 (*second edition*), vol. 10, ed. by T. Spohn, G. Schubert vol. 10 (Elsevier-Pergamon, Oxford,
1432 2015), pp. 153–193. doi:10.1016/B978-0-444-53802-4.00169-X
- 1433 M.A. Wieczorek, B.L. Jolliff, A. Khan, M.E. Pritchard, B.O. Weiss, J.G. Williams, L.L. Hood,

- 1434 K. Righter, C.R. Neal, C.K. Shearer, I.S. McCallum, S. Tompkins, B.R. Hawke, C. Peter-
1435 son, J.J. Gillis, B. Bussey, The constitution and structure of the lunar interior. Rev. Min.
1436 Geochem. **60**, 221–364 (2006). doi:10.2138/rmg.2006.60.3
- 1437 M.A. Wieczorek, G.A. Neumann, F. Nimmo, W.S. Kiefer, G.J. Taylor, H.J. Melosh, R.J.
1438 Phillips, S.C. Solomon, J.C. Andrews-Hanna, S.W. Asmar, A.S. Konopliv, F.G. Lemoine,
1439 D.E. Smith, M.M. Watkins, J.G. Williams, M.T. Zuber, The crust of the Moon as seen by
1440 GRAIL. Science **339**(6120), 671–675 (2013). doi:10.1126/science.1231530
- 1441 J.G. Williams, D.H. Boggs, Tides on the moon: Theory and determination of dissipation. J.
1442 Geophys. Res. Planets **120**, 689–724 (2015). doi:d10.1002/2014JE004755
- 1443 J.G. Williams, D.H. Boggs, W.M. Folkner, De430 lunar orbit, physical librations, and surface
1444 coordinates. IOM 335-JW,DB,WF-20130722-016, Jet Propul. Lab., Pasadena, Calif., 22 July
1445 (2013)
- 1446 J.G. Williams, D.H. Boggs, C.F. Yoder, J.T. Ratcliff, J.O. Dickey, Lunar rotational dis-
1447 sipation in solid body and molten core. J. Geophys. Res. **106**, 27933–27968 (2001a).
1448 doi:10.1029/2000JE001396
- 1449 J.G. Williams, D.H. Boggs, C.F. Yoder, J.T. Ratcliff, J.O. Dickey, Lunar rotational dissipation
1450 in solid body and molten core. J. Geophys. Res. **106**, 27933–27968 (2001b)
- 1451 J.G. Williams, A.S. Konopliv, D.H. Boggs, R.S. Park, D.-N. Yuan, F.G. Lemoine, S. Goossens,
1452 E. Mazarico, F. Nimmo, R.C. Weber, S.W. Asmar, H.J. Melosh, G.A. Neumann, R.J.
1453 Phillips, D.E. Smith, S.C. Solomon, M.M. Watkins, M.A. Wieczorek, J.C. Andrews-Hanna,
1454 J.W. Head, W.S. Kiefer, I. Matsuyama, P.J. McGovern, G.J. Taylor, M.T. Zuber, Lunar in-
1455 terior properties from the GRAIL mission. Journal of Geophysical Research (Planets) **119**,
1456 1546–1578 (2014). doi:10.1002/2013JE004559
- 1457 B.A. Wyatt, The melting and crystallisation behaviour of a natural clinopyroxene-ilmenite
1458 intergrowth. Contributions to Mineralogy and Petrology **61**(1), 1–9 (1977)
- 1459 T. Yoshino, T. Katsura, Re-evaluation of electrical conductivity of anhydrous and
1460 hydrous wadsleyite. Earth and Planetary Science Letters **337**, 56–67 (2012).
1461 doi:10.1016/j.epsl.2012.05.023
- 1462 T. Yoshino, Laboratory electrical conductivity measurement of mantle minerals.
1463 Surveys in Geophysics **31**(2), 163–206 (2010). doi:10.1007/s10712-009-9084-0.
1464 <https://doi.org/10.1007/s10712-009-9084-0>
- 1465 N. Zhao, P. Zhu, B. Zhang, Y. Yuan, Moonquake relocation. Earth Science Journal of China
1466 University of Geosciences (in Chinese) **40**, 1276–1286 (2015)
- 1467 S. Zhong, C. Qin, G. A. J. Wahr, Can tidal tomography be used
1468 to unravel the long-wavelength structure of the lunar interior? Geo-
1469 physical Research Letters **39**(15) (2012). doi:10.1029/2012GL052362.
1470 <https://agupubs.onlinelibrary.wiley.com/doi/abs/10.1029/2012GL052362>